JGR Atmospheres

RESEARCH ARTICLE
10.1029/2022JD038112

Relationship Between the Aerosol Loadings Over the Bay of Bengal and the Arabian Sea in the Early Summer and Asian Monsoon Rainfall Anomalies, and the Role of SST Anomalies in the Indian Ocean

Yongsheng Zhang[1,2], **Xuepeng Zhao**[2], **and Huai-Min Zhang**[3]

[1]Cooperative Institute for Satellite Earth System Studies/Earth System Science Interdisciplinary Center, University of Maryland, College Park, MD, USA, [2]National Centers for Environmental Information, National Oceanic and Atmospheric Administration, Silver Spring, MD, USA, [3]National Centers for Environmental Information, National Oceanic and Atmospheric Administration, Asheville, NC, USA

Key Points:

- Anomalous aerosol loadings over the Bay of Bengal concur with an out-of-phase rainfall change in South and East Asia in early summer
- Aerosol-monsoon interaction over the Arabian Sea tends to modulate Indian rainfall by changing the meridional air temperature gradient
- Sea surface temperature anomalies in Indian Ocean play an important role in stimulation of the aforementioned aerosol-monsoon interaction

Supporting Information:

Supporting Information may be found in the online version of this article.

Correspondence to:

Y. Zhang,
yongsheng.zhang@noaa.gov

Citation:

Zhang, Y., Zhao, X., & Zhang, H.-M. (2023). Relationship between the aerosol loadings over the Bay of Bengal and the Arabian Sea in the early summer and Asian monsoon rainfall anomalies, and the role of SST anomalies in the Indian Ocean. *Journal of Geophysical Research: Atmospheres*, *128*, e2022JD038112. https://doi.org/10.1029/2022JD038112

Received 4 NOV 2022
Accepted 26 MAY 2023

Author Contributions:

Conceptualization: Yongsheng Zhang
Data curation: Yongsheng Zhang
Formal analysis: Yongsheng Zhang
Funding acquisition: Huai-Min Zhang
Investigation: Yongsheng Zhang, Xuepeng Zhao
Methodology: Yongsheng Zhang, Huai-Min Zhang
Project Administration: Huai-Min Zhang
Resources: Yongsheng Zhang
Software: Yongsheng Zhang

Abstract Two relatively long-term satellite aerosol products during 1983–2020 and 2000–2020 are employed to investigate interannual relationships between anomalous aerosol loadings over the Bay of Bengal (BoB) and Arabian Sea (AS) in the early summer and Asian monsoon rainfall anomalies. It is shown that increased aerosol loading (IAL) over the BoB is primarily attributed to an intensified upstream aerosol transport by anomalous subtropical westerly winds and coincides with local sea surface temperature (SST) cooling due to intensified prevailing wind and the aerosol dimming effect, and vice versa. A deficient rainfall in India tends to concur with a BoB IAL while excessive rainfall with an AS IAL in May and June. In June, a BoB IAL coincides with significantly deficient rainfall in the southwestern China-Huaihe River Basin primarily linked to an anomalous cyclone off the coast of Southeast China. Meanwhile a related overturning of Walker Circulation is identified to be driven by the contrast of anomalous convective activity between the southeastern Indian-BoB and the South China Sea-Philippine Sea. An AS IAL is associated with air warming in North India due to an elevated aerosol semi-direct effect and remote forcing that reinforces the meridional air temperature gradient. The IAL over the respective BoB and AS in June are both preceded by cold SST anomalies in the western Indian Ocean that can be traced back to the preceding winter, but the corresponding atmospheric circulations driving aerosol-monsoon interactions differ distinctly. The above aerosol-monsoon relationships are sustained primarily during 2000–2020 and vague during 1983–2020.

Plain Language Summary The year-by-year aerosol variations over the Bay of Bengal (BoB) and Arabian Sea (AS) in early spring and their relationship to the Asian summer monsoon rainfall anomalies are studied using satellite-observed aerosol products. Increased aerosol loading (IAL) over the BoB is revealed to be accompanied by deficient rainfall in India and excessive rainfall in the northern South China Sea-Philippine Sea (NSCSPS), driven by the changes in Walker Circulation primarily caused by the contrast of anomalous convective activity between the southeastern Indian-BoB and the NSCSPS. An IAL over the AS tends to concur with excessive monsoon rainfall in India in May and June and is associated with air warming in northern South Asia partially due to the aerosol semi-direct effect that reinforces the meridional air temperature gradient. The aerosol dimming effect associated with an IAL over the BoB and AS, along with the intensified prevailing westerly, might be responsible for the cooling of the local sea surface temperature (SST) in early spring and vice versa. The SST anomaly in the western Indian Ocean, which can be traced back to the preceding winter, plays an important role in driving the aforementioned associated changes in the atmospheric circulations and monsoon rainfall anomalies.

1. Introduction

Atmospheric aerosols directly perturb the Earth's energy budget by scattering and absorbing radiation, which is named aerosol direct effect (e.g., Ohmura, 2009; Twomey, 1974; Wild et al., 2009). Aerosols can also alter the properties and lifetime of clouds by serving as cloud condensation nuclei and ice nuclei, which may further impact the radiation budget and precipitation efficiency (e.g., Albrecht, 1989; Breon et al., 2002; Coakley et al., 1987; Lohmann & Feichter, 2005), and eventually modify the energy and hydrological cycles of the Earth climate system (Ramanathan, Crutzen, Kiehl, & Rosenfeld, 2001, Ramanathan, Crutzen, Lelieveld, et al., 2001;

Validation: Yongsheng Zhang, Xuepeng Zhao
Visualization: Yongsheng Zhang, Xuepeng Zhao
Writing – original draft: Yongsheng Zhang, Xuepeng Zhao
Writing – review & editing: Yongsheng Zhang, Huai-Min Zhang

Rosenfeld et al., 2008; Seinfeld et al., 2016). These effects that aerosols have on clouds and precipitation as well as the atmospheric energy and hydrological cycles are generally called the aerosol indirect effects.

Aerosols exert large influences on climate, weather, air quality, hydrological cycles, and ecosystems on both global and regional scales directly as well as indirectly. For example, global aerosol direct and indirect effects may offset a significant part of the global warming caused by greenhouse gases (IPCC, 2021). At the same time, aerosol pollution in the Indo-Gangetic Plain and China also has a clear influence on regional Asia summer monsoon (see a general review by Li et al. (2016) and Jin et al. (2021)). Thus, long-term global and regional aerosol observations of climate quality are needed to determine the global and regional aerosol distributions and study how they are changing temporarily. The environmental and climate consequences of the aerosol changes must also be studied, particularly for those associated with anthropogenic activities. Long-term satellite aerosol climate data records for the past 40 years fit this observational need very well. This paper will study the regional scale interactions of aerosol and the Asian summer monsoon using long-term satellite aerosol observations.

South Asia, especially the Indian subcontinent and the tropical Indian Ocean, provides an ideal and unique natural laboratory for the study of the role of aerosols in climate change. As it is surrounded by oceans on three sides, anthropogenic aerosols (such as sulfate), dust particles, as well as marine aerosols (such as sea salt) are abundant over the Indian subcontinent (Jin et al., 2021; Krishnamurti et al., 1998; Li et al., 2016; Ramanathan, Crutzen, Kiehl, & Rosenfeld, 2001, Ramanathan, Crutzen, Lelieveld, et al., 2001). Dust particles mainly originate from the desert areas of Central Asia, South Asia, and Northeast Africa. Anthropogenic aerosols are mainly resulted from industrial pollution over the subcontinent, and marine aerosols are mostly from the northern Indian Ocean. In the late spring and summer, the polluted and pristine air is connected by a cross-equatorial monsoonal flow into the Intertropical Convergence Zone (ITCZ). The subtropical flow from the northeast to the southwest brings dry and polluted continental air over the ocean, which enables the pollutant-laden haze to accumulate and spread on an ocean basin scale. Long-term satellite observations also reveal an increasing trend of aerosol loadings in India, Southeast Asia, China, and their surrounding coastal oceanic areas (e.g., Jeong & Li, 2005; Li et al., 2016; Massie et al., 2004; Mishchenko & Geogdzhayev, 2007; Zhao et al., 2008), due to fast development in the economy in the last three decades and associated growth in the industrial emissions of the surrounding countries.

As one of the global monsoon systems, the Asian summer monsoon (ASM) geographically spans South Asia, Southeast Asia, and East Asia, and modulates the weather and climate variability in the regions. The ASM consists of a northward progression of the on-average zonally oriented rain belts that develop in the South China Sea (SCS) and Southern Bay of Bengal (BoB) in early to mid-May and reach northern India and northern China in later summer (e.g., Tao & Chen, 1987; Tanaka, 1992; Lau & Yang, 1997; Wang & LinHo, 2002; and many others). The annual cycle of the solar forcing and the associated thermal heating contrast between the land and ocean and changes in sea surface temperature (SST) in the Indo-Pacific Ocean is generally considered to be the most important driving mechanism for the seasonally northward migration of the heavy rainfall. As direct or indirect effects, the El Niño–Southern Oscillation (ENSO) phenomenon in climate variability on seasonal-to-interannual time scales (e.g., Chang et al., 2000b; Kumar et al., 1999; Lau & Yang, 1997; Slingo, 1999; Wang et al., 2000; Webster et al., 1998; Yasunari, 1990; many others), Indian Ocean Dipole (IOD) (Ashok et al., 2001; Li et al., 2003; Saji et al., 1999; Webster et al., 1998), as well as the anomalies of land surface processing associated with the snow cover over the Tibetan Plateau (TP) and Eurasian land (Bamzai & Shukla, 1999; Chen & Wu, 2000; Hahn & Shukla, 1976; Wu & Qian, 2003; Xu et al., 2012; Xiao & Duan, 2016; Yasunari et al., 1991; Zhang et al., 2004; Zhao et al., 2007; many others), are the primary factors underlying the interannual variations of the ASM, which are characterized by early or later arrival of the rainy season and a deficit or excessive amount of rainfall.

The possible effects of anthropogenic aerosols and dust on the behavior of the ASM have been investigated in the past few decades by observation data analysis and modeling studies on a continental or regional scale (Bollasina et al., 2011; Ganguly et al., 2012; Jin et al., 2014; Kaskaoutis et al., 2018; Lau et al., 2006, 2008; Meehl et al., 2008; Menon et al., 2002; Ramanathan et al., 2005; Vinoj et al., 2014; Wang et al., 2009; many others). The results from these studies show that aerosol absorption may result in an increase in atmospheric stability in the ocean and a decrease in SST gradients in the Northern Indian Ocean (NIO), which leads to a decrease in the north-south thermal contrast between continents and oceans and, therefore, weakening of the prevailing summer monsoon westerly and a reduction of the Indian summer monsoon, which mostly occurs in the peak monsoon season (e.g., Meehl et al., 2008; Ramanathan et al., 2005; many others). On the other hand, Lau and Kim (2006), Lau et al. (2006, 2008), Yang et al. (2022), and Jin et al. (2014, 2021) demonstrated that in the early summer

atmospheric heating by aerosol absorption over northern India and the southern Tibetan Plateau would result in water cycle feedback and, therefore, strengthen ASM. Ramanathan et al. (2005) addressed such monsoon impacts in a numerical model simulation and additionally indicated that reductions in surface solar radiation due to solar dimming causes more cooling of the northern Indian Ocean than the southern Indian Ocean, thereby weakening the latitudinal SST gradients. Independent satellite retrievals document a strong correlation between aerosol optical depth in the Arabian Sea and monsoon precipitation in central India on short timescales (Jin et al., 2014, 2015; Vinoj et al., 2014).

Though the impact of anomalous aerosol loading on the Indian summer monsoon has been simulated and investigated in a number of modeling and observational studies, the temporal-spatial distribution of the relationship among related climate factors and complex aerosol-Asian monsoon interaction still needs to be explored. Tian et al. (2008) investigated the modulation of aerosols by the Madden-Julian Oscillation (MJO) using multiple global satellite aerosol products and found large variations in the aerosol over the equatorial Indian and western Pacific Oceans where MJO convection is active. Meehl et al. (2008) showed that the anomalous cooling of SST over the Indian Ocean due to the solar dimming effect could result in an enhanced rainfall during the pre-monsoon months (March-April-May) and yet a reduced rainfall during the monsoon months (June-July-August) over South Asia. Some of the studies that used an atmospheric model with fixed SST show that aerosols contribute significantly to ocean temperature change and in turn, exert a strong impact on the change of monsoon circulation. On the other hand, while different types of aerosol may have different effects on climate variability, the distribution of aerosol loading is determined by meteorological conditions. In contrast to the aerosol sources over the land of Central Asia, South, and East Asia, the variability of the aerosol over the northern Indian Ocean has been a research-void area partially due to the unavailability of long-term observations in the ocean regions. It is of scientific importance to address the questions of what meteorological conditions contribute to the significant interannual variations of the aerosol loading and what physical processes associated with those atmospheric circulation changes impacts on the anomaly of the ASM in different stages. In order to answer these questions, different satellites products are needed so that they can be compared for validation. Additionally, the background of the interdecadal timescale still needs to be considered. Some recent studies point out that a change in an aerosol long-term trend occurs in the South Asian monsoon starting from early 2000 (Jin et al., 2021; Jin & Wang, 2017) that is accompanied by the summertime dust loading over the Arabian Peninsula (Ravi Kumar et al., 2019).

Compared to the South Asian monsoon, the time-space distribution of the interannual rainfall anomaly in East Asia primarily exhibits a significant north-south dry and wet contrast between the polar front in eastern and southeastern China and south Japan (Ding, 1992; Johnson et al., 1993; Tao & Chen, 1987). The question of how the changes of the differential surface heating by the aerosol direct effect in the Northern Indian Ocean affect the "downstream" (with respect to the direction of the summer monsoon prevailing westerlies) climate in East Asia is still poorly observed and investigated.

Given the complexity of the aerosol-atmosphere interaction and regionality of the timing for the ASM (which exhibits a continuous northward movement of the zonal rainfall belt and consists of different weather systems in different regions), the aerosol-monsoon interaction is subtle and complicated. With the help of satellite instruments that provide consistent and relatively long-term observations of aerosol loading in the atmosphere from bottom to top, we can perform a systemic investigation of the aerosol-monsoon interactions, particularly over the two key Asian monsoon ocean regions of the Bay of Bengal (BoB) and the Arabian Sea (AS), where the highest monthly aerosol loading and significant interannual variability have been observed using the 38-year long-term monthly product of the global ocean aerosol optical thickness (AOT) Climate Data Record (CDR), from Advanced Very High-Resolution Radiometer (AVHRR) satellite observations (Figure 1). In this study, emphasis is placed on exploring the interannual variability of the aerosol loading in these two regions based on the 38-year monthly AVHRR AOT products with climate quality generated by the National Centers for Environmental Information (NCEI) and the 21-year aerosol optical depth (AOD) retrieved from the Moderate Resolution Imaging Spectroradiometer (MODIS) Terra satellite, and their relationship to the anomaly of Asian monsoon rainfall during the boreal summer transitional season.

For this purpose, we first document the interannual variations of the aerosol over the BoB and the AS in May and June, respectively, and compare the results from different satellites in Section 3. Then, we analyze the relationship between anomalous aerosol loadings over the BoB and the AS and Indian and East Asian summer rainfall anomalies in Section 4. The anomalous spatial structures of the atmospheric circulation and SST changes associated

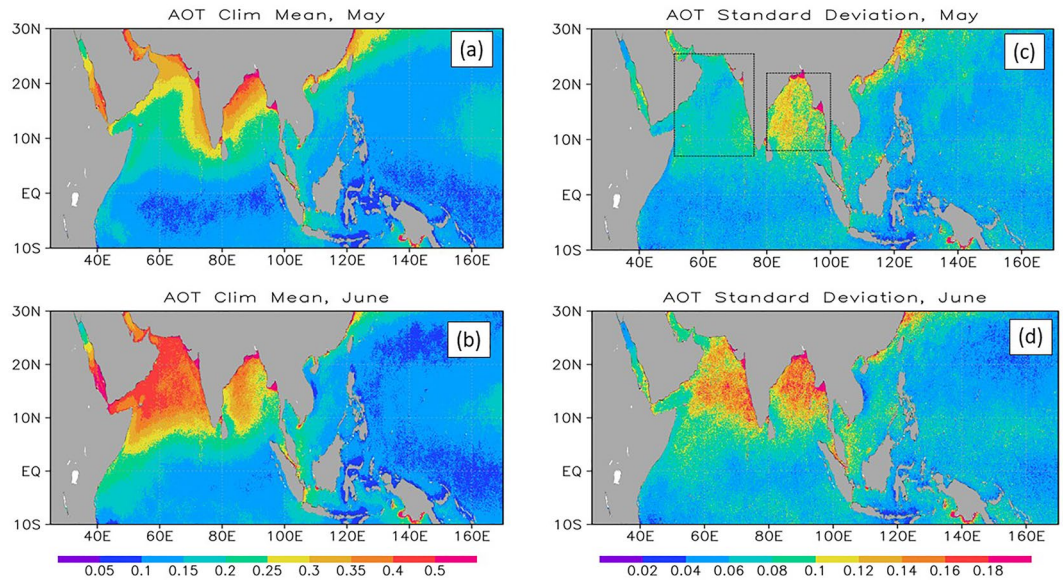

Figure 1. The long-term monthly mean of the aerosol optical thickness (AOT) from Advanced Very High-Resolution Radiometer aerosol optical thickness Climate Data Record (AVHRR AOT CDR) in (a) May and (b) June, and the standard deviation in (c) May and (d) June from 1983 to 2020. The two boxes in (c) denote the areas for the Bay of Bengal (80°E–100°E, 8°N–22°N) and the Arabian Sea (51°E–76°E, 7°N–25.5°N), respectively. The shading scale bars in a default case are applied to the figures in the same column.

with an anomalous aerosol loading over the BoB and monsoon rainfall anomaly, as well as underlying processes are explored in Section 5. Section 6 is the same as Section 5 but focuses on the Arabian Sea. In Section 7, we explore the precursory signals of SST anomaly (SSTA) in the Indian Ocean and their connections to the anomalous aerosol concentration over the BoB and AS, and ASM rainfall anomalies. Conclusions are given in Section 8.

2. Data and Analysis Procedure

2.1. NCEI Global Ocean AOT CDR From AVHRR

The AVHRR AOT CDR (Zhao & NOAA CDR Program, 2017) is derived from the Pathfinder Atmospheres–Extended (PATMOS-x) Cloud Properties CDR products in NCEI within the National Ocean and Atmospheric Administration (NOAA). PATMOS-x CDR products include a full suite of cloud and atmospheric products derived from the AVHRR sensor flown on polar-orbiting weather satellites beginning in the late 1970s and continuing through the present. They are produced by the Cooperative Institute for Meteorological Satellite Studies at the University of Wisconsin–Madison (Heidinger et al., 2014). The NCEI AOT CDR is derived from the global water (or ocean) surface at a 0.63 μm channel using a two-channel AVHRR aerosol retrieval algorithm (Zhao et al., 2004) from the AVHRR clear-sky reflectance from 1981 to present. The PATMOS-x AVHRR all-sky reflectance and cloud probability CDR products (Heidinger et al., 2014) are used to determine the clear-sky reflectance for each orbital pixel. Due to the limited channels of the AVHRR instrument, only the aerosol over water is retrieved. In addition, the retrieval from a wider 0.86 μm channel is contaminated by water vapor absorption, which is difficult to accurately quantify especially in the AOT trend detection. Because of this, only the AOT retrieved at the 0.63 μm channel achieves a climate quality. The retrieval algorithm has been validated by comparing it with the Aerosol Robotic Network (AERONET) ground AOT measurement (Zhao et al., 2003, 2004) and the MODIS satellite AOT observation (Zhao et al., 2005), which confirms the data quality and the utilization of long-term AVHRR aerosol products in climate studies. In this study, the monthly NCEI AOT CDR v3.0 product on a 0.1° × 0.1° grid from 1983 to 2020 is used.

2.2. MODIS-Aqua and Terra Aerosol Optical Depth (AOD) Product

In this study, we also use the AOD retrieved at 0.55 μm from the MODIS aboard the Terra (originally known as EOS AM-1) and Aqua (originally known as EOS PM-1) satellites. There are two MODIS monthly global

data product files: MOD08_D3 contains the data collected from the Terra (DOI: 1250 https://doi.org/10.5067/MODIS/MOD08_M3.006) and MYD08_D3 from the Aqua (DOI: 1251 https://doi.org/10.5067/MODIS/MYD08_M3.006, Platnick et al., 2015). Separate algorithms have been applied over oceans (Tanré et al., 1997) and land (Kaufman et al., 1997; Remer et al., 2005), respectively. The algorithms are continuously evaluated and periodically updated (Hsu et al., 2006; Levy et al., 2007a, 2007b; Remer et al., 2008). Collection 6.1 monthly AOD products contain combined dark target and deep blue retrievals over land and ocean on a 1° × 1° grid from February 2000 to December 2020 for Terra and from July 2000 to December 2020 for Aqua. In contrast to Terra, we use an improved version for Aqua, which is marked "best" over the ocean and "corrected" over the land. The data is downloaded from the NASA GIOVANNI website (https://giovanni.gsfc.nasa.gov/giovanni/).

2.3. SeaWiFS Aerosol Product

The third satellite aerosol data set used is the SeaWiFS aerosol optical thickness product from 1997 to 2010 (Hsu et al., 2013). Even though the SeaWiFS is primarily used for routine global ocean color measurements and ocean bio-optical property data generation due to its high accuracy in calibration and high spectral band signal-to-noise characteristics (Gordon & Wang, 1994), it also measures aerosol optical thickness and Angström components. In this study, the SeaWiFS deep blue Level 3 monthly product at 0.55 μm in a 1° × 1° spatial resolution from September 1997 to December 2010 is used. The data are downloaded from the NASA GIOVANNI website.

2.4. The Fifth-Generation Atmospheric Reanalysis of the European Centre for Medium-Range Weather Forecasts (ERA5)

The ERA5 monthly averaged data (Hersbach et al., 2019, 2020) on pressure levels and at 10 m surface on a 0.25° × 0.25° grid from 1983 to 2020 was used in this study. The changes in associated circulation are analyzed by using atmospheric parameters of air temperature, specific humidity, geopotential height, wind, and vertical velocity at various levels.

2.5. Global Precipitation Climatology Centre (GPCC) Monthly Precipitation

Operated by Deutscher Wetterdienst (DWD, National Meteorological Service of Germany), the GPCC produces monthly global land-surface precipitation from rain-gauges built on Global Telecommunication System (GTS)-based and historic data (Schamm et al., 2014). In this study, the monthly data with spatial resolutions of 1.0° latitude by longitude from 1983 to 2020 was used.

2.6. Global Precipitation Climatology Project (GPCP) Monthly Precipitation

The GPCP monthly precipitation CDR provides a consistent analysis of global precipitation from an integration of various satellite data sets over land and ocean and a gauge analysis over the land (Adler et al., 2016). In our study, the Version 3.1 monthly data on a 2.5° grid from 1983 to 2020 is downloaded from the NOAA Physical Sciences Laboratory.

2.7. The NOAA 1°/4° Optimum Interpolation SST (OISST)

The OISST is a long-term CDR generated in NOAA NCEI that incorporates observations from different platforms including satellites, ships, buoys, and Argo floats (Huang et al., 2021; Reynolds et al., 2002). In this study, the V2.1 data on a 0.25 longitude by latitude grid is used. The OISST has a temporal resolution of daily, and the data are averaged monthly in this study.

3. Comparison of Variabilities of the Aerosol Over the BoB and the AS Among Different Satellites Observations in May and June

A limited number of studies pointed out that the Northern Indian Ocean is one of the regions over the global ocean where the largest aerosol loading has been observed climatically (e.g., Li et al., 2016; Jin et al., 2021; many others). This motivates our efforts to investigate the temporal-spatial distributions of aerosol variability in the BoB and AS and aerosol-monsoon interactions through an in-depth analysis of the NCEI-produced long-term

AVHRR satellite AOT CDR. Moreover, to avoid the uncertainty of the satellite observations from different sensors, we also compare the AVHRR AOT to the MODIS AOD, which contains relatively short periods but more advanced observations.

Figure 1 shows the distributions of the long-term monthly mean of AVHRR AOT (Figures 1a and 1b) and the standard deviation (Figures 1c and 1d) during the 1983–2020 period, respectively. It demonstrates that over the Indian Ocean and West Pacific Ocean, the maximum aerosol is observed off the coast of the Indian Peninsula in May whereas minimum aerosol centers are located primarily over the tropical Indian and West Pacific Oceans between 10°S and the equator. In June, aerosols increase distinctly over both BoB and AS and display a remarkable meridional aerosol gradient, implying that aerosol transport from the land to the ocean tends to be dominant in the aerosol loading in these two regions (Figures 1a and 1b). The distribution of standard deviation shows that high variance primarily occurs over the BoB in May (Figure 1c) and appears over both AS and BoB in June (Figures 1b and 1d).

While the above different features exhibit distinct aerosol variations in May and June, the timing of the monsoon wet phase, which is associated with the aerosol rainfall wash-out effect, differs in the BoB and AS. A number of previous studies (Lau & Yang, 1997; Tanaka, 1992; Tao & Chen, 1987; Wang & LinHo, 2002) have indicated that in eastern India from early May, the timing of the South Asian summer monsoon rainfall is characterized by the northward migration of the convection center from south of the equator to the southern BoB and occurring in the southern corner of the Indian subcontinent in late May, before finally arriving in the Northern Indian Himalayan Foothills (NIHF) in late June. In the western Indian Ocean, a separate monsoonal convention center appears in early May in the equator and then moves northward and arrives in the southern Arabian Sea south of 15°N in late May, and finally reaches coastal northwestern India in late June. Therefore, in this study, we not only treat the aerosol variation in May and June, respectively, but also separate them into two regions while some common features are also summarized. Accordingly, we define two separate domain-averaged aerosol indices over the BoB (80°E–100°E, 8°N–22°N) and AS (51°E–76°E, 7°N–25.5°N), respectively. These two domains are marketed by the two black rectangle frames in Figure 1c.

Figure 2 shows the climatological annual cycle of the AOD and AOT indices over the BoB and AS from satellite aerosols of the 38-year AVHRR AOT, 21-year Terra, and 19-year Aqua AOD, as well as 11-year SeaWiFS AOT data sets. The annual variation over the BoB is exhibited by a peak in June and a low in November in the AVHRR, Aqua, and Terra data, while SeaWiFS data shows a peak in May. Over the AS, all observations consistently display a distinct peak in July and a low in December-January. Other than that, the SeaWiFS data contains a relatively smaller variance in the AS, which may be related to the saturation of the SeaWiFS observation in heavy aerosol loading conditions (Li et al., 2009).

Figure 3 displays the time series of BoB aerosol indices in May (Figure 3a) and June (Figure 3b) from different satellite observations. The AVHRR AOT (0.63 μm) varies from 0.2 to 0.4 while MODIS and SeaWiFS AOD (0.55 μm) fall in the range from 0.3 to 0.5 both in May and June. In May all the high aerosol years (e.g., 2003, 2005, 2008, 2013, and 2019 in Figure 4a) and low years (e.g., 2000, 2004, 2006, 2010, 2018, and 2020) are consistent for all products. We also provide a quantitative estimation of the strength of the relationship among the products in Table 1, which shows the correlation coefficient values of aerosol over the BoB among AVHRR AOT and MODIS AOD each month. The SeaWiFS data are not included due to its short observation period (11 years). The values between the Terra and Aqua are above 0.96 in all months, indicating the significant consistency between these two aerosol products, whereas quantitatively the values of Aqua AOD are slightly larger than those derived from Terra (Figures 3a and 3b). For the AVHRR data, May and June are the two of the best correlated months, with values of 0.91 (0.83) between the AVHRR AOT and Terra (Aqua) AOD in May, and 0.91 (0.91) between the AVHRR AOT and Terra (Aqua) AOD. August is the worst month in which correlation coefficient values drop to 0.61 between AVHRR AOT and Terra AOD, and 0.50 between AVHRR AOT and Aqua AOD. The latter only exceeds the significance level of 95% while the values in other months exceed the level of 99%.

Similarly, Figure 4 and Table 2 present the AS aerosol indices and their respective correlation coefficient values. For AVHRR AOT, a weakening of the amplitude of year-to-year variation is seen after late 1990 (Figures 4a and 4b), and its relationship to the Terra and Aqua AOD becomes weaker than those over the BoB. The correlation values between AVHRR AOT and Terra AOD, and between AVHRR AOT and Aqua AOD drop to 0.50 and 0.66 in May, and 0.58 and 0.58 in June, respectively. In the worst-correlated month of August, the AVHRR-Terra and AVHRR-Aqua correlations are only 0.23 and −0.05.

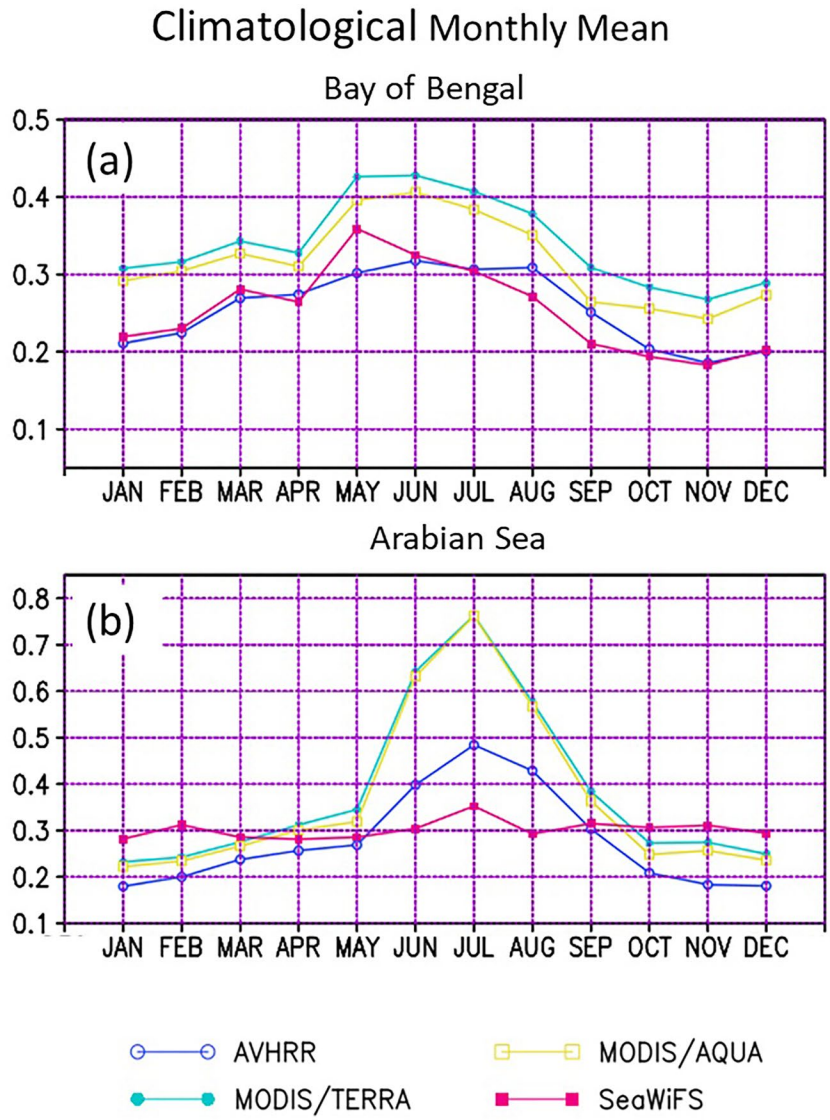

Figure 2. The time series of the domain-averaged climatological monthly mean aerosol indices calculated from Advanced Very High-Resolution Radiometer Climate Data Record (AVHRR CDR) (blue), Terra (cyan), Aqua (yellow), and SeaWiFS (red) over the (a) Bay of Bengal (BoB) (80°E–100°E, 8°N–22°N) and (b) the Arabian Sea (51°E–76°E, 7°N–25.5°N) areas which are denoted in Figure 1c.

The above difference might be caused by a couple of reasons. The spatial resolution of heritage AVHRR observation (~4 km) is lower than that of advanced MODIS observation (~0.5 km) and MODIS also has more observational spectral channels compared to AVHRR (36 channels vs. 5 channels). Thus, the cloud detection and screening scheme based on MODIS observation is more accurate than that of AVHRR, especially during the cloudy and rainy monsoon season. As a result, AVHRR observation may miss more aerosol detection, especially in some heavy aerosol scenarios due to relatively strong transport associated with vigorous monsoon dynamic and thermodynamic processes. This is the major cause for the relatively large difference between AVHRR and MODIS aerosol observation during the peak monsoon months (July and August). The cloud detection and screening effect on aerosol retrieval is small in the dry pre-monsoon season, which is the major reason that we focus our study on May and June rather than the peak monsoon months.

Lacking spectral channels for AVHRR aerosol retrieval relative to MODIS retrieval may also impact the final AOT values. However, this impact from the difference in the AVHRR and MODIS aerosol retrieval algorithms is mainly over land. Actually, the AOT differences caused by the aerosol retrieval algorithm of AVHRR to that of

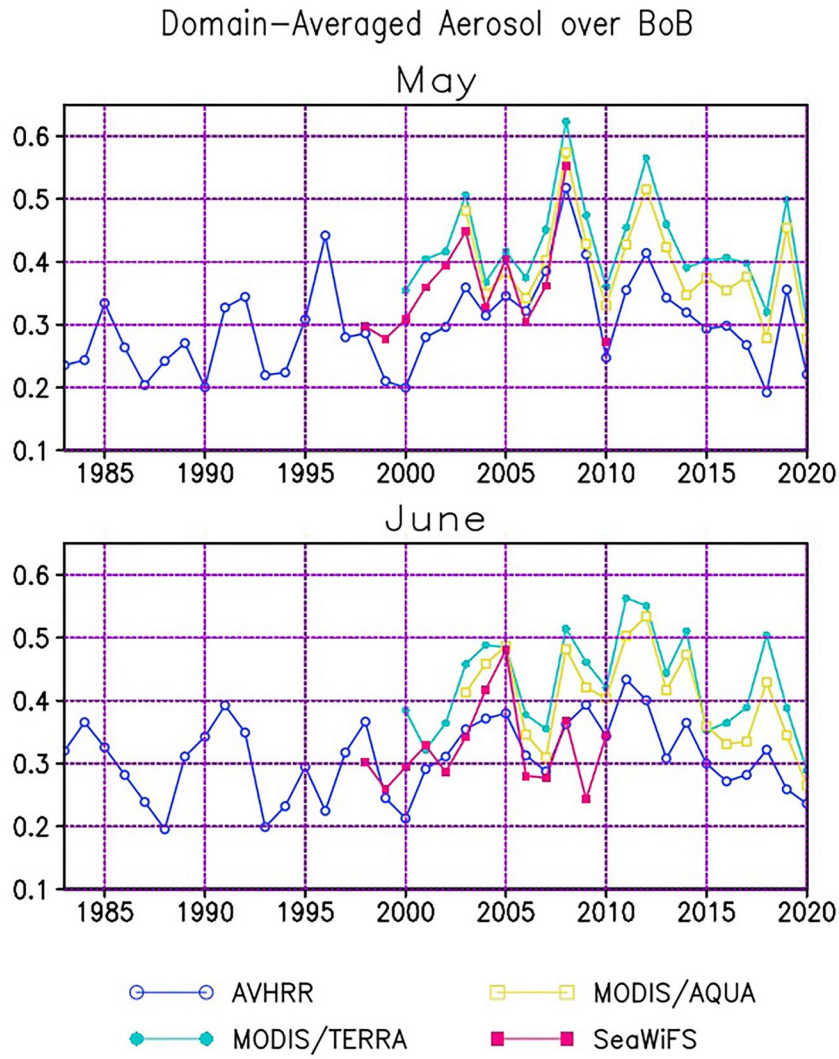

Figure 3. The time series of the domain-averaged aerosol indices calculated from Advanced Very High-Resolution Radiometer aerosol optical thickness Climate Data Record (AVHRR AOT CDR) (blue), Terra (cyan), Aqua (yellow), and SeaWiFS (red) over the Bay of Bengal (BoB) in (top) May and (bottom) June.

MODIS over the ocean are relatively smaller (Li et al., 2009; Zhao et al., 2005). MODIS radiometric calibration uncertainties in reflectance (±2%) are also more accurate than that of AVHRR (±5%), which may result in a large difference in AOT retrievals. However, AVHRR reflectance has been cross-calibrated with MODIS before using for deriving AOT CDR, which brings the AVHRR calibration uncertainty close to that of MODIS (Cao et al., 2008; Heidinger et al., 2002, 2010) and minimizes the impact on the AOT retrieval caused by the calibration uncertainties.

For a further comparison of aerosol data derived from different satellite missions and revealing the spatial distribution patterns associated with the domain-averaged indices over the receptive BoB and AS, we calculate the correlation coefficient between the aerosol indices and itself or other satellite 2-dimensional aerosol fields, respectively. As the MODIS/Aqua product provides a quality-improved aerosol data set over both land and ocean during 2003–2020, here we can extend our analyses from the ocean to land. Among the correlation maps, Figure 5 presents the self-correlations between the AVHRR AOT BoB and AS indices and its 2-dimensional fields (left panels) and those between the Terra AOD indices and Aqua AOD fields (right panels) during 2003–2020. The color shading areas where values are larger than 0.47 or smaller than −0.47 indicate an exceeding of the 95% confidence level. We can see the correlation patterns of AVHRR based AOT and its indices over BoB and AS are generally similar to those of MODIS based AOD and its indices in both May and June. It is notable that because

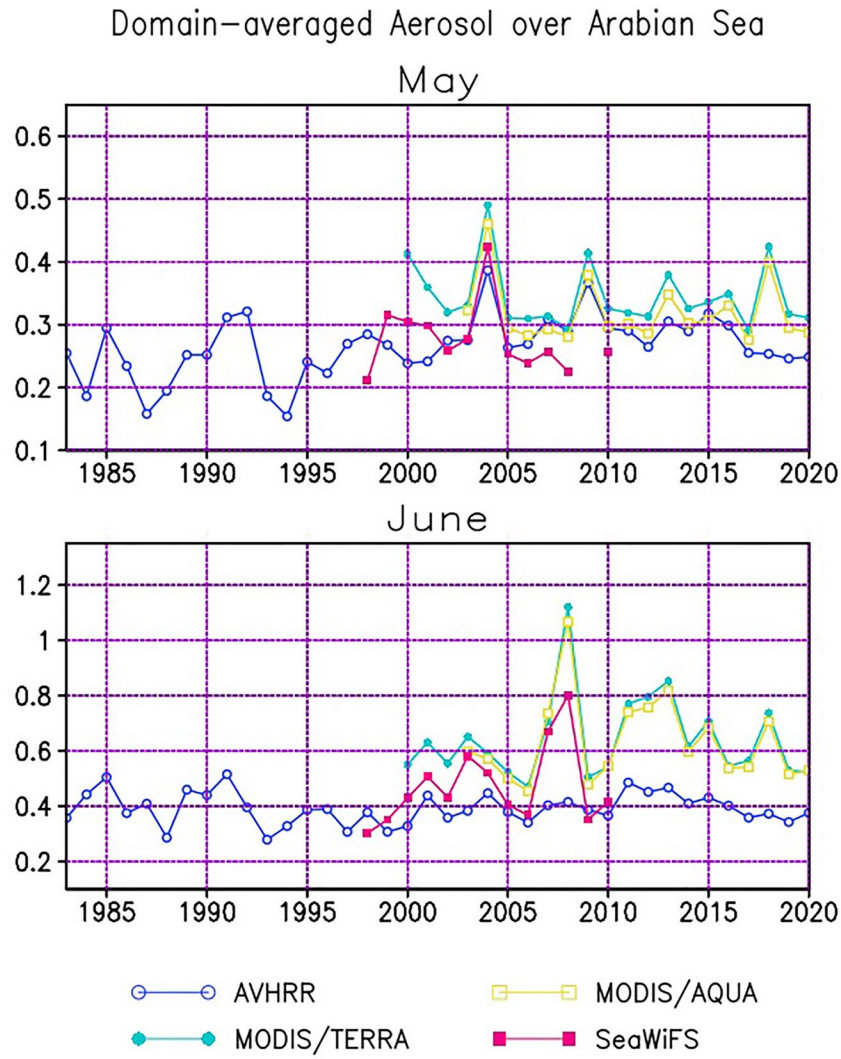

Figure 4. Same as Fig. 3, but for the Arabian Sea.

the correlation coefficient values between Terra and Aqua AOD indices over the BoB are 0.96 and 0.98 in May and June (Table 1), and 0.99 and 0.99 over the AS in May and June (Table 2), respectively, the right panels, whereas they are the correlations between Terra aerosol Index and Aqua aerosol fields, are very similar to those of Terra and Aqua self-correlations which have not been shown.

Examining in details, Figures 5a and 5b show that an increased aerosol loading over the BoB is accompanied by an aerosol increase in the downstream SCS and the marginal seas of East Asia as well as the northwestern Pacific Ocean and vice versa. Furthermore, the self- or cross-correlations between Terra and Aqua data sets display remarkable out-of-phase variations between the BoB and AS in May in Terra and Aqua data sets (Figure 5e and ignored figures) and high negative correlations in the southern Indian Ocean south to 10°S (Figures 5e and 5f). Increased loading in the downstream regions is not observed for an increased aerosol loading over the AS in May (Figures 5c and 5g), whereas it is concurrent with a significant increase of aerosol in central Africa between 10°S to 10°N in the Aqua data (Figure 5g). The AVHRR AOT self-correlations in June (Figure 5d) exhibit a broad positive correlation band extending from the Arabian Sea, the southern BoB, SCS, and tropical west Pacific Ocean, implying that aerosols dwelled over the AS are transported to broader downwind areas by monsoon flow in June than in May. This monsoon flow transport is also noticed in the distribution of Terra and Aqua AOT cross-correlation in Figure 5h. As the correlation coefficient between AVHRR AOT and Aqua (Terra) AOD indices over the AS is 0.58 (0.58) in June (Table 1), some differences between Figures 5d and 5h are expected, and the

Table 1
Correlation Coefficient Values of Monthly Aerosol Over the Bay of Bengal (BoB) Among Advanced Very High-Resolution Radiometer Aerosol Optical Thickness (AVHRR AOT), Aqua, and Terra Aerosol Optical Depth (AOD)

	January	February	March	April	May	June	July	August	September	October	November	December
AVHRR–TERRA (2000–2020)	**0.65**	**0.71**	**0.72**	**0.75**	**0.91**	**0.83**	**0.82**	**0.61**	**0.84**	**0.77**	**0.89**	**0.88**
AVHRR–AQUA (2003–2020)	**0.66**	**0.77**	**0.72**	**0.77**	**0.91**	**0.91**	**0.84**	0.50	**0.83**	**0.73**	**0.79**	**0.77**
TERRA–AQUA (2003–2020)	**0.99**	**0.99**	**1.00**	**0.99**	**0.96**	**0.98**	**0.97**	**0.98**	**0.98**	**0.98**	**0.98**	**0.96**

Note. Values exceeding the 99% confidence level are shown in bold.

latter presents relatively weaker signals in the BoB and marginal seas of Southeast Asia for an increased aerosol loading over the AS in June. Overall, the above evidence indicates that large-scale aerosol spatial distributions correlated to the aerosol loading over the BoB and AS differ distinctly. An increased aerosol loading over the BoB is apparently accompanied by a distinct increase of the aerosol in Southeast and East Asia and adjacent ocean regions far extending to the middle West Pacific Ocean, suggesting that the aerosol-monsoon interactions over the BoB and AS are likely dominated by different circulation patterns and are consistent with what we uncover in the following sections. It is also notable that in June the correlation between the AOD index over the AS and the aerosol observed by Aqua is highly positive over the land regions in the northwestern India (Figure 5h) along the western Himalayan foothills, reflecting a concurrency of aerosol increase in the region. This consistently provides a possible cause of overlapped air warming by the semi-direct aerosol effect which will be further discussed with other atmospheric parameters later.

4. Relationship Between Anomalous Aerosol Loadings Over the BoB and AS and Summer Rainfall Anomalies in South and East Asia

The evidence identified in the above section confirms that the annual and interannual variations of the aerosol over the BoB and AS regions observed by the AVHRR and MODIS satellites are consistent each other. In the subsequent studies, we start by investigating the relationship between the interannually anomalous aerosol loadings over the BoB (and AS) and the Asian monsoon rainfall anomalies in the early summer. In the first step, we compute the correlations between precipitation and aerosol indices of the Terra AOD and AVHRR AOT during 2000–2020, and then also calculate those with respect to the AVHRR AOT indices during 1983–2020. Considering that the primary monsoonal rainfall belts sit in different locations during the summer monsoon transitional period (May and June), we perform the above analysis in May and June separately.

4.1. Relationship of the Aerosol Loadings Over the BoB and Asian Summer Monsoon Rainfall Anomalies

Figure 6 presents the correlations of the GPCC or GPCP precipitation with respect to the Terra AOD index over the BoB during 2000–2020 and to the AVHRR AOT index during 1983–2020. It is shown that there exists a significantly negative correlation between aerosol loading over the BoB and rainfall in South Asia extending from central and northeast India to Bangladesh-northern Myanmar in May (Figure 6a) during 2000–2020. In Southeast Asia, a high positive correlation is visible in the southern Indochina peninsula covering Cambodia and south Vietnam, as well as the northern Philippines. In June, a negative northwest-southeast-tilted tongue is observed in central India between 15°N to 20°N latitude (Figure 6b). In Southeast and East Asia, the correlations display a conspicuous northeast-southwest-oriented teleconnection pattern in which positive correlations are visible primarily in the northern Indochina peninsula and northwestern Korea while significant negative correlations occupy a larger area extending from Southwest China to the Huaihe River Basin.

As a combined precipitation data set from an integration of various satellite data sets in the ocean and gauge analyses over land, the GPCP precipitation, though containing a coarser grid resolution compared to GPCC data, is very helpful in the investigation of the related tropic convective activity. The GPCP precipitation exhibits a correlation pattern similar to that of GPCC over the land in South and East Asia. It also reveals considerably negative correlations in the southwestern BoB and on the coast of the southwestern Indian subcontinent, as well as the region zonally covering the southeastern Indian Ocean between 10°S and the equator with an extension to central Indonesia (Figure 6c). In the SCS and the west Pacific Ocean, a northeast-southwest-oriented zone of positive correlations extends from the central SCS, the Philippine Sea and the North Pacific Ocean, to the south of Japan (Figure 6c). In Figure 6d, compared to those of GPCC, the GPCP-AOD index correlation maps in June exhibit a conspicuous north-south-oriented teleconnection pattern in Southeast and East Asia. Consistently, a significant positive correlation center appears in the northern SCS-Philippines Sea and is accompanied by a negative one in the southern SCS-central Indonesia with a westward extension along 5°N and reaching 85°E in the tropic eastern Indian Ocean (Figure 6d).

To confirm the results from MODIS/Terra AOD data, we also compute the correlation between the GPCC and GPCP precipitation and AVHRR index over the BoB during 2000–2020 as shown in Figure S1 in Supporting Information S1. One can see that the correlation maps of rainfall to the two satellites' aerosol data are quite similar, and both capture the prominent features including deficient rainfall along the regions spanning northeastern India, Bangladesh and northern Myanmar (Figure S1a in Supporting Information S1), intensified convective

Table 2
Same to Table 1, But for the Aerosol Over the Arabian Sea

	January	February	March	April	May	June	July	August	September	October	November	December
AVHRR–TERRA (2000–2020)	**0.72**	**0.72**	**0.78**	**0.72**	0.50	**0.58**	0.52	0.23	**0.70**	**0.70**	**0.81**	**0.67**
AVHRR–AQUA (2003–2020)	**0.73**	**0.66**	**0.82**	**0.63**	**0.66**	0.58	0.46	−0.05	**0.77**	**0.63**	**0.73**	0.54
TERRA–AQUA (2003–2020)	**0.99**	**0.99**	**0.99**	**0.99**	**0.99**	**0.99**	**0.99**	**0.99**	**0.99**	**0.99**	**0.99**	**0.98**

Note. Values exceeding the 99% confidence level are shown in bold.

activity in the southwestern BoB and a teleconnection intensified rainfall pattern along the western North Pacific Ocean in May (Figure S1c in Supporting Information S1). However, the negative correlation between AVHRR AOT and GPCC is relatively a little bit weaker compared to the Terra AOD index on the coast of the southwestern India (Figure 6a and Figure S1a in Supporting Information S1). In June, prominent deficient monsoon rainfall in the Indian subcontinent and China ranging from the southwest region to the Huaihe River Basin, and significant seesaw changes of convection between southern SCS and the northern SCS-Philippine Sea are documented consistently (Figure 6d and Figure S1d in Supporting Information S1).

For a longer time period of 1983–2020, the negative correlations between aerosol loading over the BoB and rainfall in South Asia spanning central and northeast India, Bangladesh and northern Myanmar are still dominant in May (Figure 6e), but the signals in central-eastern India are relatively weaker (Figure 6f) in June. In Southeast Asia, high positive correlations are visible in the Indochina Peninsula primarily sitting in the southern region in May and in the northeastern one in June, while a dry-wet meridional contrast between the tropic Indonesia-Malaysia and subtopic northern Philippines can also be seen in May and June during 1983–2020 (Figures 6e and 6f). In East Asia, the area of remarkably negative correlations in China identified during 2000–2020 is mainly located over a smaller domain of 30°N–38°N and 100°E–110°E during 1983–2020, and the positive correlations over the northeastern China-northern Korea are much stronger (Figure 6f).

In summary, our correlation analyses for both AVHRR and MODIS aerosols reveal that in the early summer, though strength and locations might be slightly different from May to June, an increased anomalous aerosol loading over the BoB tends to be negatively related to monsoon rainfall in South Asia and to be concurrent with suppressed convective activity in the eastern tropic Indian Ocean and an intensified convective activity in the SCS-Philippine Sea. It is notable that deficient rainfall observed in the regions spanning the northeastern India, Bangladesh, and the northern Myanmar in May and the central and southern India subcontinent in June might imply a dry or delayed arrival of the summer Indian monsoon in the regions and vice versa. In Southeast and East Asia, a north-south-oriented rainfall teleconnection pattern is dominant with alternating signs propagating from the equator to the middle latitude in Asia, and a distinct dry (wet) phase of rainfall extending from Southwest China to the Huaihe River Basin occurs in June.

4.2. Relationship of the Aerosol Loading Over the Arabian Sea and the Asian Monsoon Rainfall Anomalies

Figure 7 presents the correlation between the MODIS Terra AOD index over the AS and monthly GPCC and GPCP precipitation during 2000–2020, respectively. Figure 7a shows that a high positive center is primarily observed in the South India and Northeast Indochina Peninsula in May. In June, significant positive correlations are visible primarily in North India along the Himalayan foothills and Northeastern China, while a weak positive correlation center can also be seen on the coast of Southeast China as well as a negative one in Southwest China (Figures 7b and 7d), exhibiting a seesaw change pattern of rainfall anomalies. Compared to that of GPCC in Figure 7a, the GPCP-aerosol correlation map in Figure 7c displays a larger positive correlation area in South India in May which extends to the eastern Arabian Sea, and a high correlation center in the southern Indian Ocean at 10°S and 80°E.

We also calculate the correlations between the AVHRR AOT index over the Arabian Sea and GPCC and GPCP precipitation during 2000–2020. The results are shown in Figure S2 in Supporting Information S1. The significant positive correlations in South India in May and North India along the Himalayan foothills in June in Figure 7 are consistently observed in Figure S2 in Supporting Information S1, whereas the size of domains in Figure S2 in Supporting Information S1 is relatively smaller than those in Figure 7. Comparatively, the results of AVHRR AOT index also displays a small negative zonal tongue in the Huaihe River Basin in June, which is located to the south of the maximum center in Northeast China (Figure S2b in Supporting Information S1). Additionally, a high negative correlation is also identified along the equator over Malaysia and Indonesia in Figure S2b in Supporting Information S1 as part of the southwest-northeast-oriented teleconnection pattern in the marginal seas of the western Pacific Ocean (Figure S2d in Supporting Information S1).

Figures 7e and 7f display the correlation maps between the GPCC precipitation and the AVHRR AOT index over the AS during 1983–2020 in May and June, respectively. While the positive correlation still can be seen in South India in May in Figure 7e, the significant positive correlations in North India along the Himalayan foothills reduce in June in Figure 7f in contrast to those in Figures 7b and 7c.

In summary, analyses of both AVHRR and Terra aerosol products reveal that an increased (decreased) aerosol loading over the Arabian Sea tends to be concurrent with a wet (dry) monsoon rainfall in the Indian subcontinent

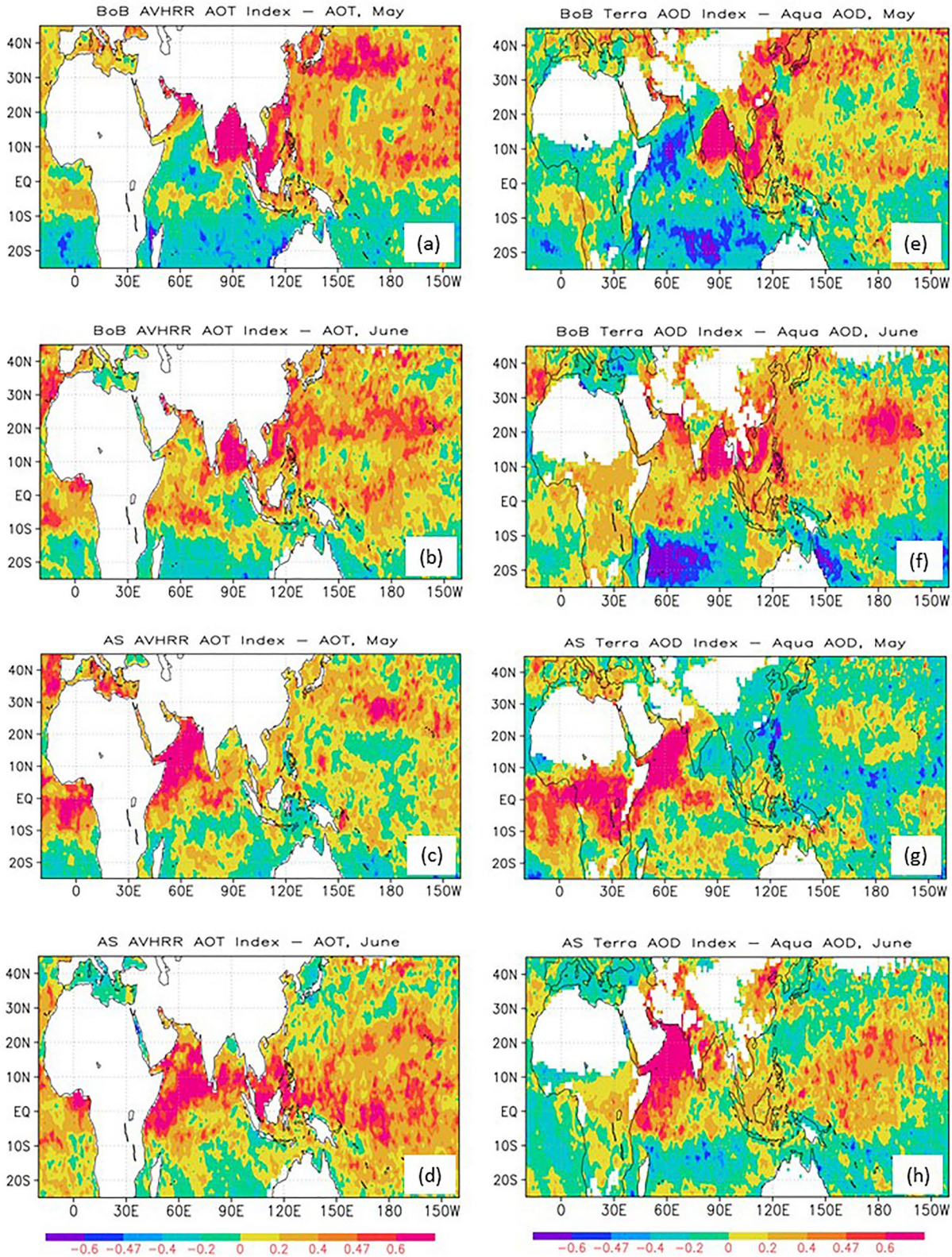

Figure 5. The self-correlations between the Advanced Very High-Resolution Radiometer aerosol optical thickness (AVHRR AOT) domain-averaged indices (over the Bay of Bengal (BoB) and the Arabian Sea (AS)) and AVHRR AOT fields (left panels): (a) BoB index in May, (b) BoB index in June, (c) AS index in May, (d) AS index in June, and the correlations between the MODIS/Terra AOD indices (over the BoB and AS) and Aqua AOD data which are observed over land and ocean during 2003–2020 (right panels): (e) BoB index in May, (f) BoB index in June, (g) AS index in May, (h) AS index in June. The color shading areas where values are larger than 0.47 or smaller than −0.47 indicate an exceeding of the 95% confidence level.

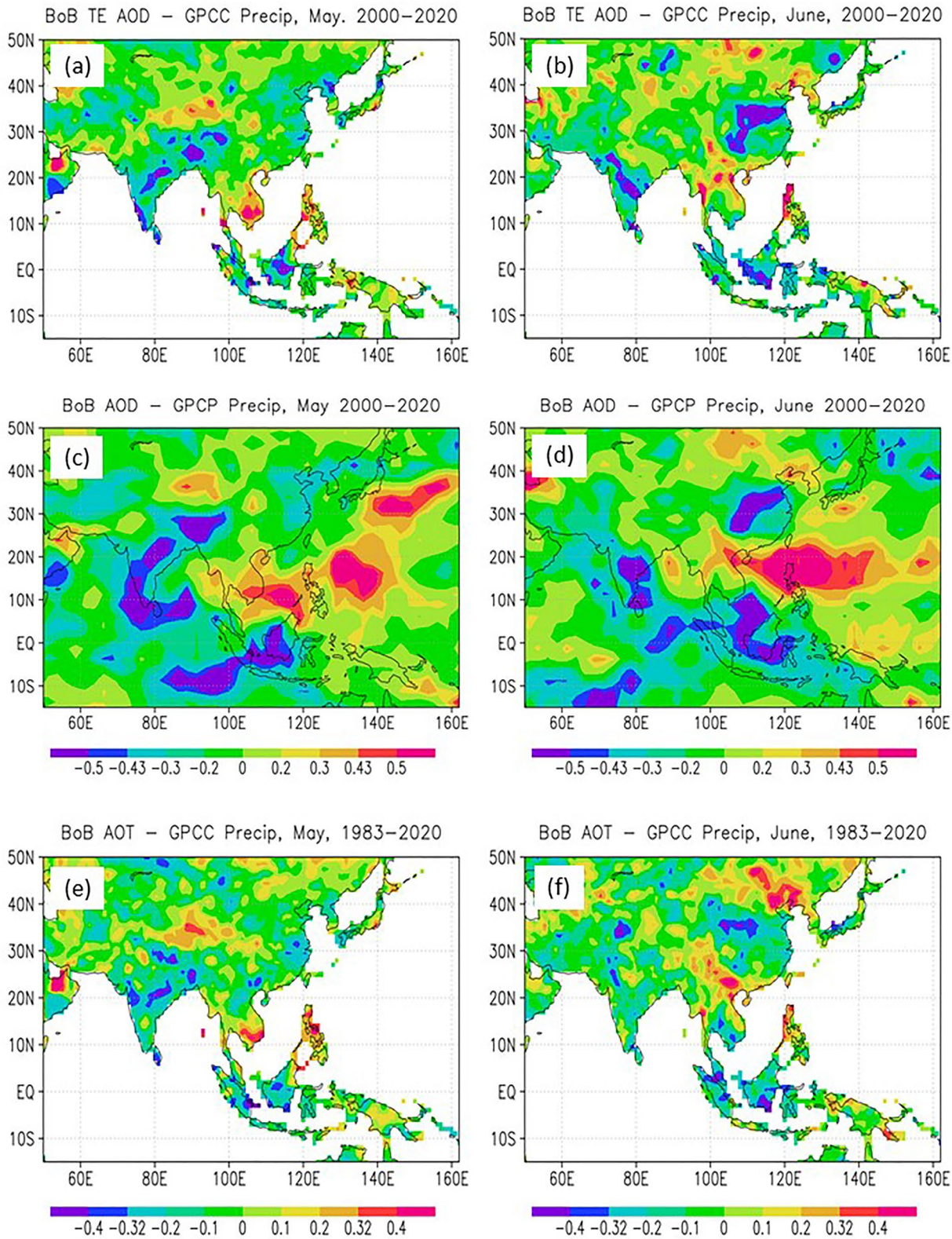

Figure 6. The correlation coefficient between the MODIS/Terra aerosol optical depth (AOD) index over the Bay of Bengal (BoB) and monthly precipitation of (a) Global Precipitation Climatology Centre (GPCC) in May, (b) GPCC in June, (c) Global Precipitation Climatology Project (GPCP) in May, and (d) GPCP in June during 2000–2020, and between Bay of Bengal Advanced Very High-Resolution Radiometer aerosol optical thickness (BoB AVHRR AOT) index and precipitation of GPCP in (e) May and (f) June during 1983–2020. The shading areas with values larger than 0.43 or smaller than −0.43 during 2000–2020, and larger than 0.32 or smaller than −0.32 during 1983–2020 are exceeding the 95% significance.

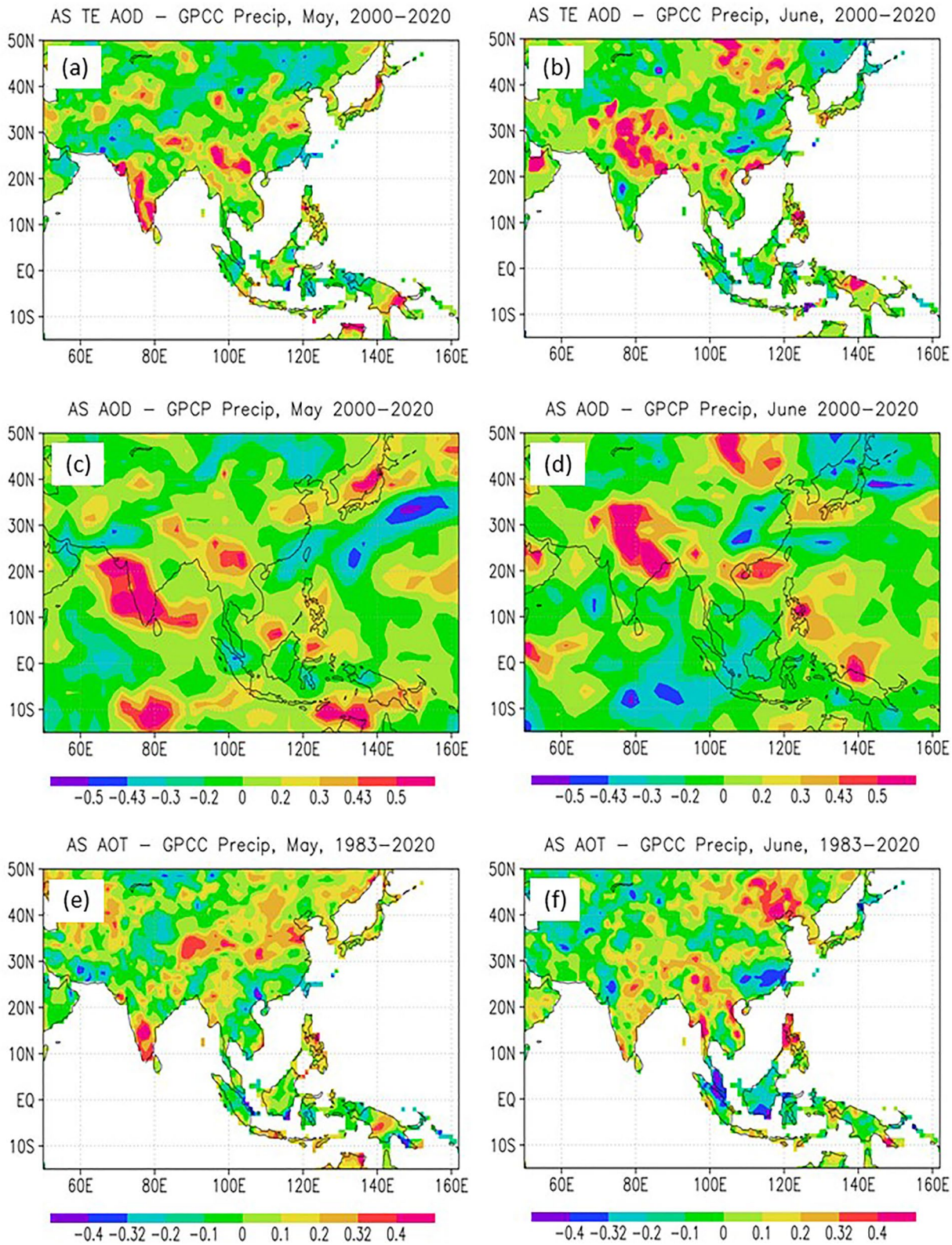

Figure 7. Same as Fig. 6, but with respect to the MODIS/Terra aerosol optical depth index averaged over the Arabian Sea.

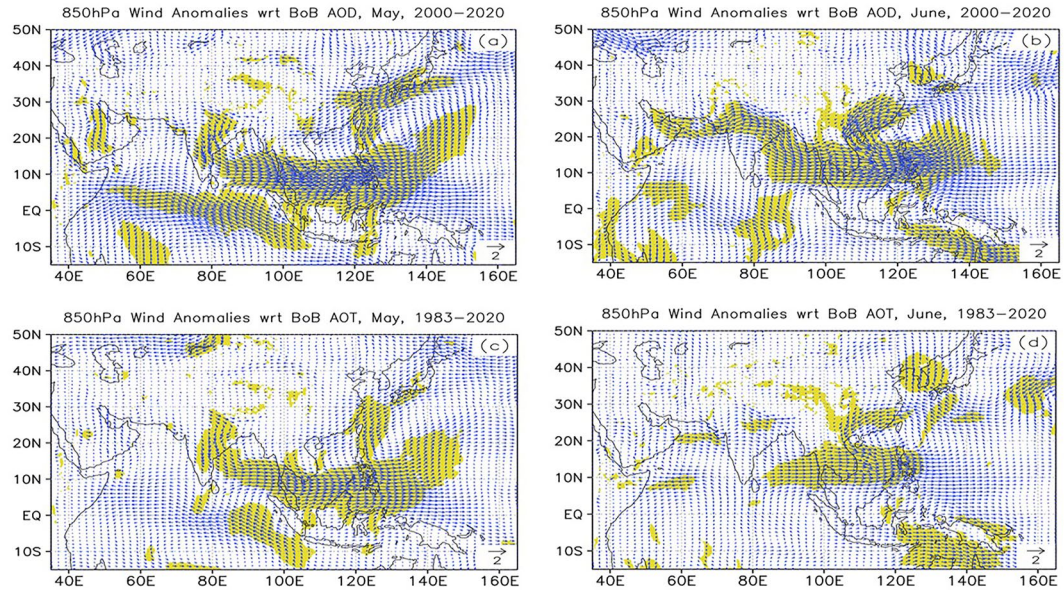

Figure 8. Regression of the wind anomalies with respect to the Terra aerosol optical depth (AOD) index over the Bay of Bengal (BoB) at 850 hPa in (a) May and (b) June during 2000–2020, and to the Advanced Very High-Resolution Radiometer aerosol optical thickness (AVHRR AOT) index over the BoB at 850-hPa in (c) May and (d) June during 1983–2020. Shading areas denote those correlations of AOD or AOT index and u or v component at 850 hPa exceed the 95% significance. The wind scales are displayed at the low right corners in a unit of ms^{-1}.

whereas the location of maximum might be different from May to June. However, the relationship becomes weaker when the time period before 2000 is included, especially in North India in June. It is also notable that compared to the correlation results between rainfall and the aerosol over the BoB (Figures 6c and 6d), the relationship between rainfall in East Asia and the aerosol over the Arabian Sea is relatively weaker.

5. Atmospheric Circulation and SST Changes Associated With the Anomalous Aerosol Loadings Over the BoB

To understand the possible connection between the ASM and an anomalous aerosol loading over the BoB, we calculate the correlations of the ERA5 wind, height, and air temperature, and SST data sets to the aerosol indices over the BoB in May and June, respectively.

5.1. Variation of the Wind, Height, Air Temperature, and SST Fields

Figure 8 displays the regression of the 850-hPa wind anomalies with respect to the Terra AOD during 2000–2020 and AVHRR AOT indices over the BoB during 1983–2020, respectively. In May (Figure 8a), it is shown that, for an increased aerosol loading over the BoB, most regions of the Indian subcontinent are under control by anomalous northwesterly or northerly winds that change to westerly ones in the southern BoB, leading to a deepening of the Bay of Bengal Trough (BBT) along the coast of East India. This broad zonal belt of anomalous westerly winds visibly spans the southern BoB, the southern SCS and the Philippine Sea. In the tropical Indian Ocean, a remarkable basin-wide anti-clockwise monsoon gyre is observed containing a southeast-northwest-tilted band of anomalous southeasterly winds ranging from 60°E to 100°E longitude and between 10°S and 8°N latitude, and northeasterly or northerly winds in the Southwestern Indian Ocean to the west of 70°E. The former and northern neighboring westerly wind belts produce strong convergences along the southern BoB near 10°N. In East Asia, an anomalous cyclone appears offshore the coast of Southeast China with its center located in the northern Philippine Sea, and associated anomalous northeasterly winds are visible over the northwestern Philippine Sea, the East China Sea, and the southern portion of the Japan Sea.

In June (Figure 8b), an increased aerosol loading in the BoB is associated with the development of the anomalous northwesterly winds not only in North India including most of the Indo-Gangetic Plain and Thar Desert regions but also in the North AS and neighboring land regions. In Southeast and East Asia, similar to that in Figure 8a, an

anomalous westerly winds belt is dominant in the BoB and the southern Southeast Asia in Figure 8b. However, they can be located further north than these regions in May and cover the southern Indochina peninsula, the central SCS, and the northern Philippines (Figure 8b) as does the anomalous cyclone offshore the coast of southeastern China. As a result, the associated anomalous northeasterly winds are observed prevailing on the coast of southeastern China while anomalous southeasterly winds are steadily seen in the Korean peninsula and the southern portion of Japan Sea. In the tropical Indian Ocean, the basin-wide anti-clockwise monsoon gyre retreats southwestward and anomalous northeasterly winds develop primarily along the coast of eastern Africa while cross-equatorial southerly winds are visible between 80°E and 95°E.

To compare the results observed from different satellites, we also produced the regressed 850-hPa wind anomalies with reference to the AVHRR AOT over the BoB during 2000–2020 and shown in Figure S3 in Supporting Information S1. In May, comparing Figure S3 in Supporting Information S1 to Figure 8a, the anonymous southeasterly winds in the tropical Indian Ocean which are associated with the anti-clockwise monsoon gyre and anomalous cyclonic winds associated with the anomalous cyclone offshore the coast of Southeast China depicted in Figure S3a in Supporting Information S1 are relatively weaker in those derived by Terra AOD data in Figure 8a whereas most of the features of the anomalous weather system are similar to each other. In June, the regressed 850-hPa winds with respect to the AVHRR AOT index (Figure S3b in Supporting Information S1) show that there exist strong anomalous northeasterly winds along the coast of eastern Africa to west of 60°E and weak cross-equatorial southerly winds between 80°E and 95°E.

Figures 8c and 8d display the regression of the 850-hPa wind anomalies with respect to the BoB AVHRR AOT indices during 1983–2020 in May and June, respectively. Compared to those that have been revealed during 2000–2020 in May (Figure 8a and Figure S3a in Supporting Information S1), the tropical anonymous southeasterly winds in the tropical Indian Ocean associated with the anti-clockwise monsoon gyre are much weaker and stronger signals can only be seen near the coast of the northwestern Sumatra. The strong anomalous northwesterly winds in North India, North AS, and Northwest BoB depicted in June in Figure 8b and Figure S3b in Supporting Information S1 weakened remarkably during the 1983–2020 periods (Figure 8c), and so do the anomalous cyclonic winds associated with the anomalous cyclone on the coast of Southeast China. Those may partially explain why the relationship between the aerosol loading over the BoB and monsoon rainfall in South Asia and East Asia is weaker than it was from 2000 to 2020 (Figures 6b and 6f).

We also compute the correlations of the aerosol indices over the BoB from AVHRR AOT and Terra AOD to the height and vertical velocity (Omega) fields at 500 hPa, and specific humidity at 700 hPa during 2000–2020. Because the results between AVHRR AOT and Terra AOD data are quite similar, Figure 9 only presents the results for the Terra AOD indices during 2000–2020. In May (Figure 9a), minimum correlations between 500-hPa height and Terra AOD index over the BoB are revealed over northern India and the central SCS-Philippine Sea. In June (Figure 9b), significantly negative correlations of height can be identified in the southwestern TP and northern SCS. Considering that climatically during boreal spring cold and dry northwesterly winds prevail over India and are concurrent with the existence of TP topographic trough (TPTT) in southern TP and the adjacent regions (Wu et al., 2013, 2014), a decrease of the 500-hPa height in northern India and the BoB benefits the development of a deep TPTT and strengthened circumferential westerly winds. Also, a decrease of the 500-hPa height in the SCS and the Philippine Sea reflects a weakening and eastward retreat of the western North Pacific subtropical high which has a significant effect on droughts, heat waves, and tropical cyclone tracks over East Asia and the northwest Pacific and will be further discussed in the later subsections.

Gandham et al. (2020, 2022) point out that climatically an eastward zonal transport of dust primarily appears within a layer between 850 and 700 hPa in the Indian Subcontinent during summer. Here the humidity-aerosol correlation maps at 700-hPa show a distinct dry-wet contract between the Indian Peninsula-west BoB and the SCS-Philippine Sea in May (Figure 9c), and between central India and the SCS-Philippine Sea in June (Figure 9d), respectively. The dry atmospheric conditions in the Indian subcontinent not only help more local aerosol emissions but also reduce the rainfall-washing effect in aerosol transport over the upstream regions of the BoB.

The distributions of correlations between 500-hPa vertical velocity and aerosol over the BoB (Figures 9e and 9f) exhibit a similar pattern to the 700-hPa humidity (Figures 9c and 9d). Namely, a descending motion, presented by a significantly positive correlation, tends to coincide with a dry condition in India-BoB regions, and a strong arising motion, corresponding to a high negative correlation, is concurrent with a wet condition in the SCS-Philippine Sea. Moreover, if we compare those features of humidity and vertical motion to the low and upper-level wind

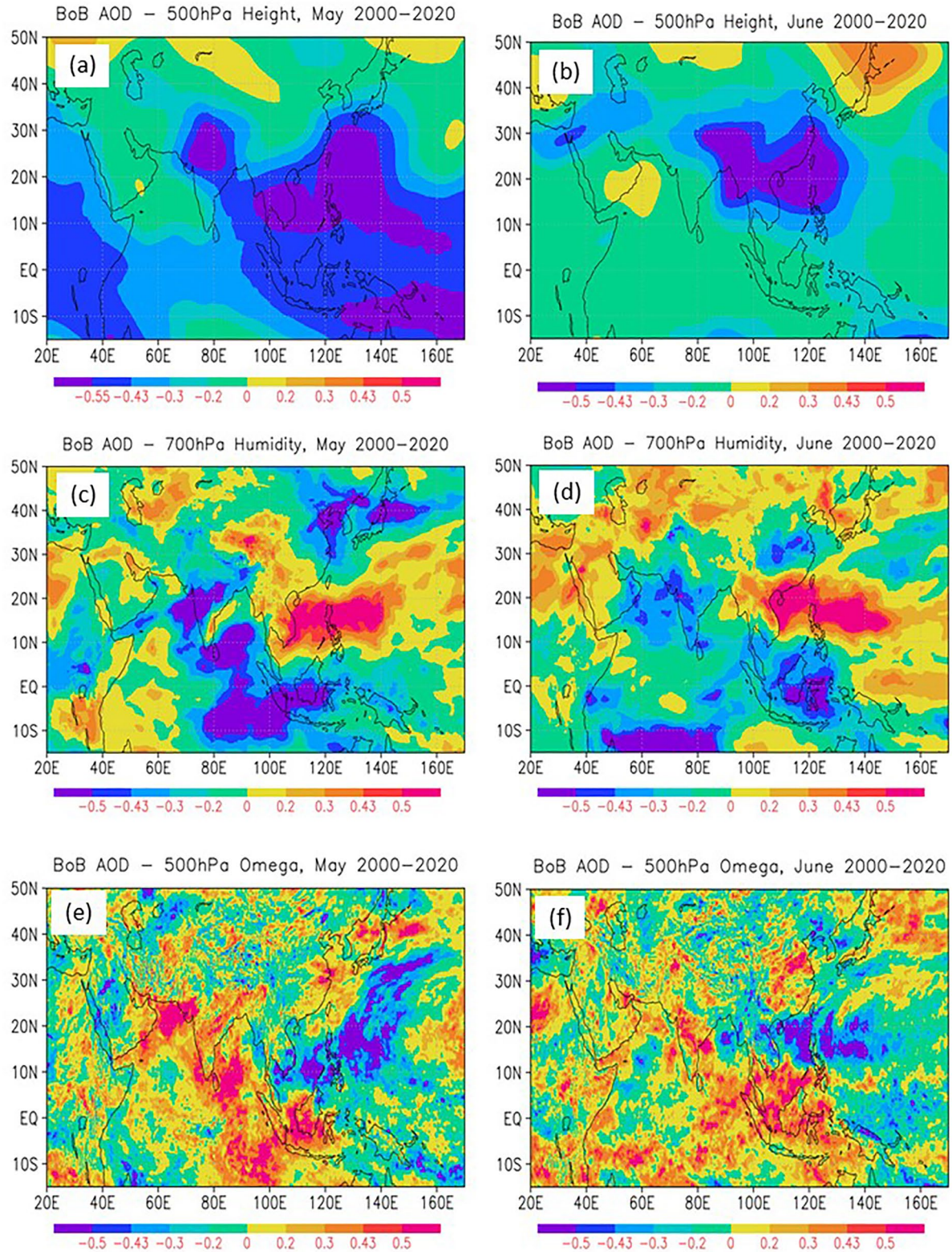

Figure 9. Correlation between the Terra aerosol optical depth (AOD) index over the Bay of Bengal (BoB) and the 500-hPa height (a) in May and (b) June, 700-hPa humidity in (c) May and (d) June, and 500-hPa vertical velocity in (e) May and (f) June. The shading areas with values larger than 0.43 or smaller than −0.43 are exceeding 95% significance.

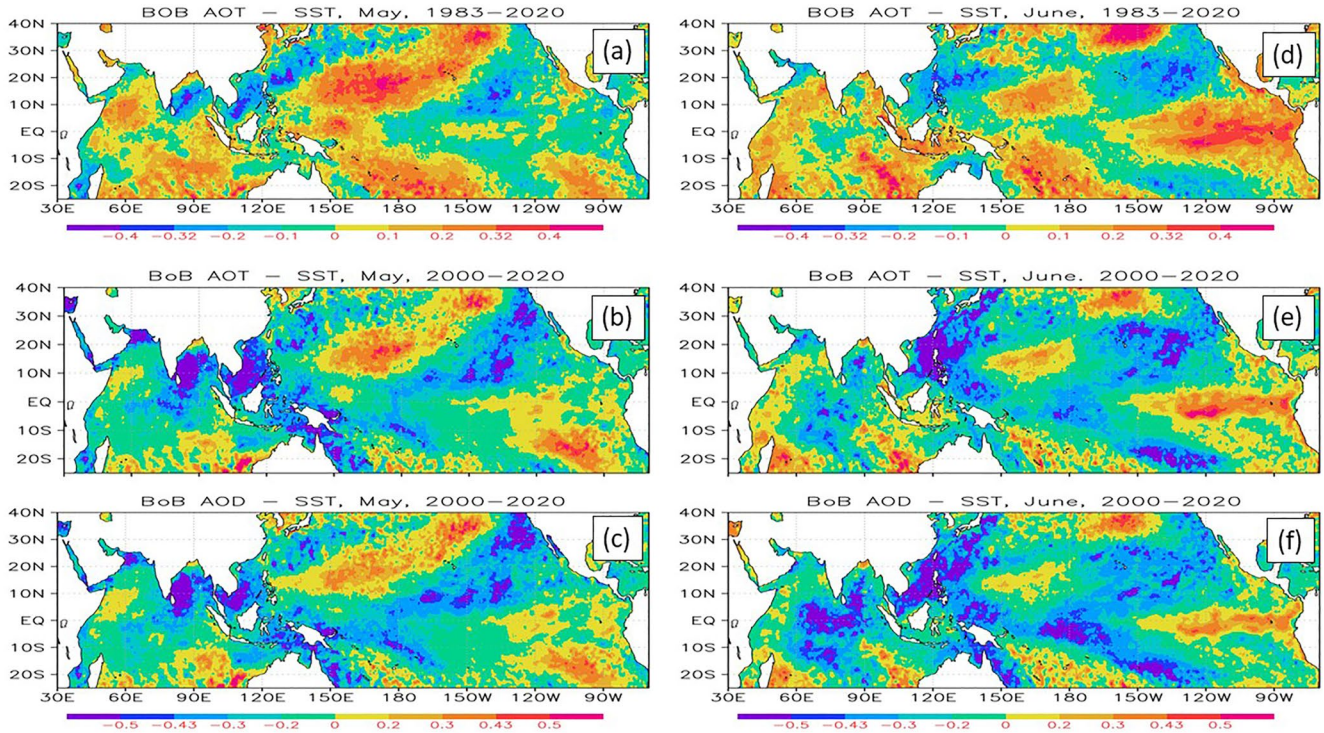

Figure 10. The correlation coefficient between sea surface temperature (SST) and (a) Advanced Very High-Resolution Radiometer aerosol optical thickness (AVHRR AOT) over the Bay of Bengal (BoB) in May during 1983–2020, (b) AVHRR AOT over the BoB in May during 1983–2020, (c) Terra AOD over the BoB in May during 2000–2020, (d) AVHRR AOT over the BoB in June during 1983–2020, (d) AVHRR AOT over BoB in June during 2000–2020, and (f) Terra AOD over BoB in June during 2000–2020. The shading areas with values larger than 0.32 or smaller than −0.32 during 1983–2020, and larger than 0.43 or smaller than −0.43 during 2000–2020 are exceeding the 95% significance.

anomalies, we can find that the concurrence of the anomalous 850-hPa westerly (Figure 8) and 200 hPa easterly winds (Figure S4 in Supporting Information S1) in the tropical Indian Ocean plays an important role in building up a bridge between these two separate regions. Furthermore, to the south of the strong ascending branch in the SCS-Philippine Sea, notable positive correlations are also visible in the southeastern Indian Ocean and southern SCS-Java Sea and imply a strong descending motion and precipitation deficiency (Figures 6c and 6d). Considering the existence of the 850-hPa cross-equatorial flows in the longitude domain from 100°E to 110°E and 120°E to 130°E in May (Figures 8a) and 120°E to 140°E in June (Figure 8b), they consistently indicate the strengthening of the Hadley Circulation in the marginal seas of the western Pacific. Most importantly, the associated highly positive correlations observed in the East Asia regions between 22°N and 40°N latitude (see Figures 9e and 9f) imply that the Hadley Circulation may play a dominant role in the modulation of far northward-positioning monsoon rainfall anomalies in East Asia.

Figure 10 presents correlation maps between SST and AVHRR AOT indices over the BoB during the two periods, and the Terra AOD during 2000–2020, respectively. In May the correlation between SST and aerosol over the BoB was highly negative in the BoB and the southern SCS during 2000–2020 (Figures 10b and 10c), while the signals are relatively weaker during 1983–2020 (Figure 10a). Apparently, the cold SST almost overlaps with the anonymous low-level westerly winds in the regions (Figures 8a and 10a and 10b). Positive correlations are observed in a southwest-northeast-oriented band in the West Pacific Ocean with paralleling negative cells to its two sides during two time periods (Figures 10e and 10f), but their values are reduced both for AVHRR AOT and Terra AOD data during 2000–2020. Negative correlations are presented in the maritime continent both for AVHRR AOT and Terra AOD data during 2000–2020 but are absent during 1983–2020. As shown in Figure 1, high AOT values have also been observed over the AS, BoB, and the seas surrounding the maritime continent, which may result in an enhanced surface radiative dimming effect. As a result, SST becomes cooler and convective precipitation may be inhibited, which is consistent with the above correlation analysis between AOT and precipitation (Figure 6c). The upward motion anomaly (Figure 9e) over the SCS-Philippine Sea due to the

overturning of the Walk Circulation seems to overpower the SST cooling in the SCS-Philippine Sea and maintain accordingly a positive correlation between AOT and precipitation (see Figure 6c).

In June, negative correlations are still visible in the northern SCS and the Philippine Sea during 1983–2020 (Figure 10d) though the signals are relatively weaker than those in May. Noticeable positive correlations can also be identified in the eastern equatorial Pacific during 1983–2020, but reduced during 2000–2020 (Figures 10e and 10f), especially for the Terra AOD data (Figure 10f). They also become much weaker compared to those in May. During 2000–2020, significant negative correlations occurred in the SCS and elongated from the northern Philippine Sea, the Yellow Sea, and the East China Sea to the northwestern Pacific Ocean south to Japan.

In the northern Indian Ocean and the BoB, no noticeable signal of SST-aerosol correlations is visible during 1983–2020 with respect to the AVHRR AOT index (Figure 10d), but during 2000–2020, Terra AOD data presents a stronger negative correlation to the SST in the central equatorial Indian Ocean which also intrudes northward into the central BoB (Figure 10f). These signals can also be seen in the correlation to the AVHRR AOT index though the signals are much weaker.

Figure 10 demonstrates that an increased aerosol loading in the BoB is concurrent with a cold SST anomaly in the BoB, implying that the aerosol dimming effect due to the anomalous aerosol loadings might cool the local SST, and vice versa. In the boreal early summer on the other hand, the prevailing wind over the BoB is southwesterly, so the anomalous westerly winds strengthen the prevailing wind (Figures S5b and S5d in Supporting Information S1), this may trigger stronger offshore ocean current and strengthen upwelling, thus, leading to stronger SST cooling (Wu et al., 2012).

5.2. Physical Processes Underlie the Aerosol-Monsoon Interactions in the BoB and Their Relationship to Asian Summer Monsoon Rainfall Anomalies

5.2.1. Favorable Environmental Circulation for an Anomalous Aerosol Loading Over the BoB

Based on the evidence presented in the previous subsections, we will explore further the dominant circulation changes underlying an increased (decreased) aerosol loading in the BoB and its relationship to the Asian summer rainfall. The first question we want to answer is what kind of circulation is favorable for an increased or decreased aerosol loading over the BoB. According to previous studies (Gandham et al., 2020, 2022; Ravi Kumar et al., 2019) summertime dust loading over the Arabian Peninsula tends to occur in the low-level atmosphere. At first, Figure 8 reveals that the northwesterly or northerly winds from the Indian subcontinent provide a direct dispersing of the continental aerosols to the coastal oceans, especially during 2000–2020 in May (Figure 8a), and produce strong convergence with the southeasterly winds from the tropic Indian Ocean to the southwest BoB associated with the anomalous basin-wide anti-clockwise monsoon gyre. This is also confirmed by the correlation maps between the meridional component of 10-m surface wind and Terra AOD index in which two neighboring high correlation centers with opposite signals are observed in India and the western BoB, respectively (Figures S5a and S5b in Supporting Information S1). The development of the BBT along the northwestern coast of India where anomalous winds change direction from northerly or northwesterly to westerly also dynamically trapped the transported aerosol. Compared to what happened in May, although the convergence over the southwestern BoB is reduced due to the weakening of the southeasterly winds to its south in June (Figure 8b and Figure S5c in Supporting Information S1), strong low-level aerosol transport is primarily exhibited by intensified westerly winds crossing from the northern Arabian Sea to the Indian subcontinent (Figure 8b and Figure S5d in Supporting Information S1).

A dry atmospheric background in the upstream regions, indicated by strong negative correlations to humidity (Figures 9c and 9d), also greatly favors an increased emission of aerosol in the Indian subcontinent and Arabian Peninsula while the strengthening of the subtropical westerly winds enhances the aerosol transport. Additionally, as the prevailing surface winds are westerly in the BoB in May and June, the high positive correlations between surface wind speed and aerosol index (Figures S5b and S5d in Supporting Information S1) indicate a strong increase in wind speed and this intensified surface prevailing flow can also contribute to more local aerosol emissions (Madhavan et al., 2008; Moorthy & Satheesh, 2000).

5.2.2. Physical Processes Underlie the Monsoon Rainfall Anomalies in May

Our correlation analyses show that for an increased aerosol loading over the BoB, an anomalous descending motion with suppressed convective activity in the southwestern BoB is concurrent with an ascending motion

with intensification of convective activity in the south SCS and Philippine Sea in May (Figures 9e and 6c). They are also accompanied by anomalous westerly winds at 850 hPa (Figure 8a) and easterly winds at 200 hPa (Figure S4a in Supporting Information S1) between these two regions along about 10°N longitude. This observational evidence is presented to show an overturning of the east-west Walker Circulation in the subtropical Asian monsoon region.

Besides the zonal remote forcing associated with the change of Walker circulation on suppressed convective activity in the southwestern BoB, the following contribution is also remarkable. The regression fields of 850-hPa wind with reference to the BoB aerosol indices display an anti-clockwise monsoon gyre in the Indian Ocean basin between 10°S and 8°N (Figures 8a and 8c). The associated southeasterly winds to the east of 70°E and easterly or northeasterly winds along the eastern African coast remarkably weaken or delay the arrival of cross-equatorial southerly or southwesterly winds along the coast of eastern Africa to the Indian subcontinent. These result in the cutting down of the transport of warm and moist air toward India which is necessary for heavy monsoon rainfall, which also leads to suppressed convection in the southwestern BoB.

On the other hand, the correlations between the aerosol index over the BoB and precipitation reveal a chain of high negative centers along northeastern India, Bangladesh, and northern Myanmar in May (Figures 6a and 6c). These regions almost overlapped with a northeast-southwest-oriented band of positive correlation between vertical velocity and BoB aerosol indices and implies the control of the weak descending motion in these regions (Figure 9c), and therefore, leading to deficient rainfall.

Considering the timing of the summer monsoon in the region, the SSTA in the BoB seems also to play an important role. The practical timing of the ASM in May is characterized by a northwestward migration of the monsoonal convection center from the southeastern BoB to land in South Asia (Wang et al., 2001; Wang & Lin, 2002; Wu & Zhang, 1998). In the BoB, the in situ cold SSTA can effectively reduce the temperature and humidity of the atmospheric boundary layer by reducing latent and sensible heat exchange between the ocean and atmosphere as well as turbulent mixing in the boundary layer. As a result, a delayed northward migration or reduction of the amount of monsoon rainfall might be caused in the BoB and neighboring northeastern India and Bangladesh. This is supported reversely by the studies of Wu et al. (2012, 2014) which reveal that a strong springtime SST warm pool in the eastern-central BoB tends to benefit a generation of the monsoon vortex which can lead to the onset of the ASM.

A conspicuous feature of East and Southeast Asia in May is the anomalous cyclone that stretches southeast-northwestward from the central SCS to the northeastern Philippine Sea while associated anomalous northeasterly winds occur in the East China Sea and westerly winds in the southern SCS-Philippine Sea to its south. A significant SST cooling (Figures 10a–10c) in the southern SCS is likely associated with the strong anomalous surface southwesterly winds (Figures 8a and 8c). Therefore, enhanced convective activity is observed in the central SCS-Philippine Sea, North West Pacific Ocean to southeast Japan (Figure 6c).

5.2.3. Physical Processes Underlie the Monsoon Rainfall Anomalies in June

Compared to that in May, for an increased aerosol loading over the BoB, the intensified convective activity in the SCS-Philippine Sea regions become more zonal-oriented and migrated further north to the region between 10°N and 20°N latitude, and a deficient rainfall is mainly located in the Indian subcontinent from 10°N to 20°N (Figures 6b and 6d). Similar to that in May, these observations, along with the anomalous wind fields at 850 and 200 hPa (Figure 8b and Figure S4b in Supporting Information S1) suggest the existence of overturning of the Walk Circulation which exerts considerable impacts on the seesaw changes of the monsoon rainfall anomalies between these two regions. An anomalous anti-clockwise monsoon gyre observed in the central-western Indian Ocean (Figure 8b), which reflects the weakening of southwesterly cross-equatorial flows offshore the coast of eastern Africa, is directly attributed to deficient monsoon rainfall in the southern part of the Indian Peninsula.

In East Asia, to the north of the intense convection activity in the northern SCS and the Philippine Sea, an anomalous cyclone is observed at 850 hPa on the coast of southeastern China with its location primarily confined to the northern SCS (Figure 8b). As a response, anomalous northeasterly winds develop in South and Southwestern China which result in a noticeable reduction of the prevailing southwesterly winds, and, thus, directly leads to a deficient summer monsoon rainfall over southwestern China and Huaihe River Basin (Figures 6b and 6d) by strongly reducing the moisture supply from BoB and SCS.

The existence of the anomalous anticyclone in the 850-hPa wind field offshore the coast of southeast China has been documented as one of the important components in stimulating the interannual variability of the Asia

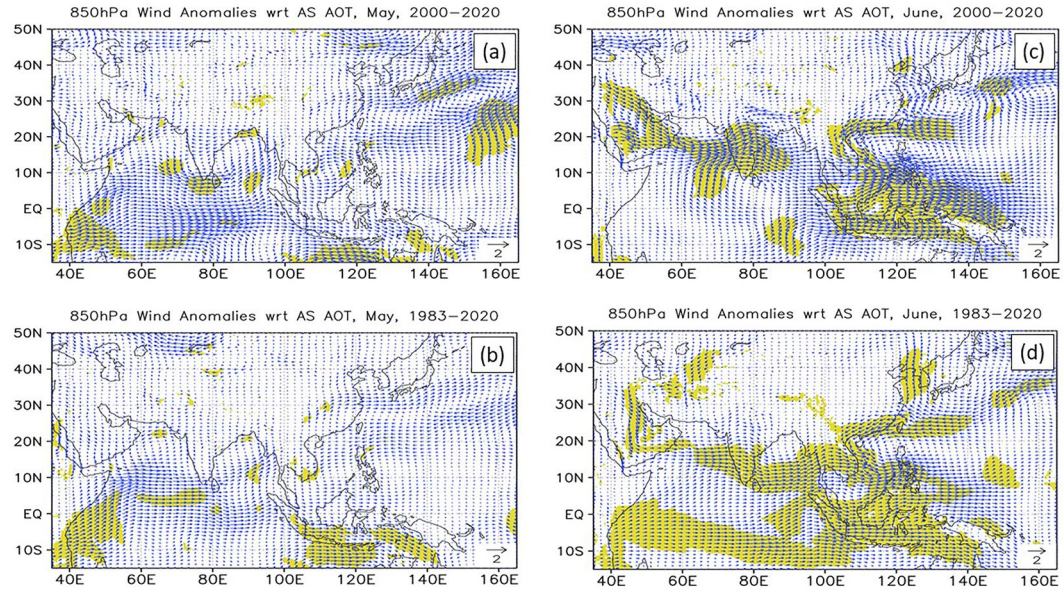

Figure 11. Regression of the 850-hPa wind anomaly with respect to the Advanced Very High-Resolution Radiometer aerosol optical thickness (AVHRR AOT) over the Arabian Sea in (a) May during 2000–2020 and (b) May during 1983–2020, (c) June during 2000–2020 and (d) June during 1983–2020. Shading areas denote those correlations of AOT index and u or v component at 850 hPa exceed the 95% significance. The wind scales are displayed at the low right corners of each panels in a unit of ms^{-1}.

summer monsoon in China (Chang et al., 2000a, 2000b; Wang et al., 2000 and others), whereas the associated location and strength of rainfall might differ slightly. In these studies, the trigger of the anticyclonic or cyclonic is primarily attributed to the SST anomalies in the western and central-eastern Pacific Ocean, as well as the intensity and location of the western North Pacific subtropical high. In our study, which is consistent with the above ones, the anomalous cyclonic circulation in the SCS is accompanied by a warming SST in the western and equatorial eastern Pacific Ocean but its strength is not as strong as those in the previous studies. We present that such anomalous cyclonic circulation tends to be triggered by the combination of a number of factors from the intense convection activity to its south, the eastward retreat of the western North Pacific subtropical high implied by the negative correlation in the SCS and the Philippine Sea at 500 hPa (Figure 9b), as well as a strong cold SST in the SCS (Figures 10e and 10f). A weakened and eastward retreat of the west North Pacific subtropical high is also favorable for a southward invasion of the extratropical cool air masses, reflecting the mixed tropical and baroclinic properties of the East Asian monsoon (Chen & Chang, 1980; Chang et al., 2000a, 2000b). It is notable that despite the above conclusions being primarily drawn for the time period 2000–2020, the changes in general circulation patterns associated with the Walk and Hadley circulations are similar to those during 1983–2020 and play a dominant role in the determination of the strength and location in monsoon rainfall anomalies.

6. Atmospheric Circulation and SST Changes Associated With the Anomalous Aerosol Loadings Over the Arabian Sea

6.1. Variation of the Wind, Height, Air Temperature, and SST Fields

Figures 11 and 12 present regressions of 850 and 200-hPa wind anomalies with reference to the AVHRR AOT and MODIS AOD indices over the AS during the periods of 1983–2020 and 2000–2020, respectively. It is shown that in May an increased aerosol loading observed by the AVHRR instrument is concurrent with two weak anomalous cyclonic cells over the AS and BoB, respectively (Figures 11a and 11b), and the resulting low-level convergence favors the aerosol accumulation over the AS during both two time periods. To the south of the cyclonic cells, significantly anomalous cross-equatorial southwesterly winds are visible offshore the coast of eastern Africa which turn to the northwesterly in tropical northern India. Compared to those observed from AVHRR data, the wind anomalies regressed from the Terra AOD index display stronger anomalous cyclonic cells over the AS and southwesterly cross-equatorial flows (Figure 12a). The above evidence indicates that the accumulation of the aerosol is mainly contributed to by sources from both the Arabian Peninsula and the coast of eastern Africa.

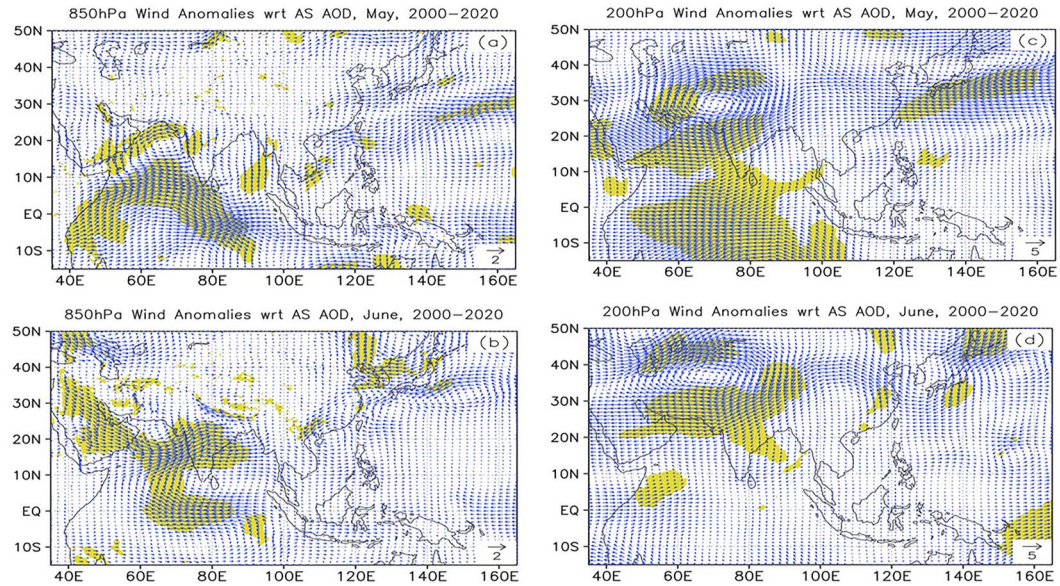

Figure 12. Regression of the wind anomalies with respect to the Terra aerosol optical depth (AOD) index over the Arabian Sea at 850 hPa in (a) May and (b) June, and at 200 hPa in (c) May and (d) June during 2000–2020. Shading areas denote those correlations of AOD or aerosol optical thickness (AOT) indices and u or v component at 850 hPa exceed the 95% significance. The wind scales are displayed at the low right corners in a unit of ms^{-1}.

In June, strong anomalous northwesterly winds are readily visible extending from the Arabian Peninsula to southeastern AS (Figures 11c and 11d and 12b) and turning to westerly or southwesterly along the coast of East AS. During 2000–2020, strong southwesterly reaches the Indo-Gangetic Plain and southeasterly is also seen along the Himalayan foothills, implying the strengthening of the monsoon trough in the regions (Figures 11c and 12b). Meanwhile, a clockwise monsoon gyre can be identified in the northern central Indian Ocean offshore the corner of South India, and associated intensified anomalous southeasterly winds flow northward from the central equatorial Indian Ocean and converge into the southeastern AS between 65°E and 75°E. But during 1983–2020 (Figure 11d), the anomalous westerly wind belt is limited to south of 20°N and a trough is seen southward-located along the coast of Southwest BoB and the convergent southwesterly from the equatorial Indian Ocean is very weak while the aforementioned clockwise monsoon gyre disappears. The difference in strength and location of convergence of the southwesterly winds to the Indian subcontinent from the AS and neighboring ocean regions, which is associated closely with the moisture supply, provide a reasonable explanation for why the interannual relationship between the aerosol loading over the AS and Indian monsoon rainfall is relatively weaker in June during 1983–2020 shown in Figure 7e. A couple of recent studies (Jin & Wang, 2017; Sanap & Pandithurai, 2014) identified that Indian monsoon rainfall has increased since early 2000 while a summertime dust amplification appears over the Arabian Peninsula (AP) starting from 2000 (Ravi Kumar et al., 2019). The facts all consistently imply that the interdecadal background needs to be taken into account in studying the aerosol-monsoon interactions in the past four decades.

In Southeast and East Asia, the AVHRR AOT index exhibits considerable circulation variations related to the anomalous aerosol accumulation over the AS (Figures 11c and 11d), but those features are shown vaguely in those related to the Terra AOD index (Figure 12b). The AVHRR AOT index regressed wind fields display the prevailing of the anomalous westerly winds in the Maritime Continent and the existence of an anomalous cyclone in northern SCS during both periods of 1983–2020 and 2000–2020. Strong anomalous easterly winds are associated with the cyclone and can be clearly seen along the coast of southeastern China, which is favorable for deficient rainfall in southwestern China (Figure 7f and Figure S2b in Supporting Information S1). The reduction of the consistency between the AVHRR and MODIS Terra observed aerosol over the AS in May and June can be also noticed in Table. 2, which shows that the correlation coefficients between AVHRR AOT and Terra AOD are 0.50 and 0.58 in May and June, respectively. Comparatively, those values are 0.91 and 0.83 in May and June over the BoB, respectively (Table 1).

While the issues discussed in the above two paragraphs indicate that the importance of interdecadal background in the aerosol-monsoon interactions, as well as disparities between different satellite observations are both subjects deserving of further investigation, neither are the primary focus in this study. In the following discussions, the proposed mechanism is mainly applied in those during 2000–2020.

To depict details of the structures of anomalous circulation, we also present the regressions of 200-hPa wind anomalies with reference to the MODIS AOD indices over the AS in Figures 12c and 12d, and their correlations to the 500-hPa height, air temperature, and vertical velocity (Omega) in Figure 13. At 200 hPa, an anomalous anticyclone is identified in northwestern South Asia in May (Figure 12c), and then shifts northward from 30°N to 35°N in June along 65°E, sitting over southeastern Central Asia (Figure 12d). Associated anomalous northeasterly winds are visible in central India and the AS in May and over the TP and the northern India in June, thereby leading to a strong upper-level divergence in the eastern part. In May, strong anomalous easterly winds are also observed in the equatorial Indian Ocean.

A notable low-pressure tongue, indicated by the significantly negative correlations, is situated in the southern AS (Figure 13a) in May while a weak high-pressure center is visible over the Indus Plain (IP) and Thar Desert regions. The anomalous middle-level low height benefits the development of the anomalous low-level cyclonic circulation along the coast of South India and the adjacent regions (Figures 11b and 12a). Similarly, in June the appearance of anomalous low-pressure in the eastern portion of North India (Figure 13b) helps the development of the trough over the IP and induces the anomalous low-level southwesterly winds which flow into the central Indian Peninsula (Figures 11d and 12b).

Figure 13 shows that the Terra-observed aerosol index over the AS has a significantly positive correlation to the 500-hPa air temperature in a zonal-oriented region of central-western India covering the southern IP and Thar Desert in May (Figure 13c) and a meridional-oriented area covering the upper Gangetic Plain and West TP along the Himalayan foothills in June (Figure 13d), respectively, while a negative correlation is observed in the southern AS along 10°N, especially in June. Associated with the above air temperature variations in May, strong ascending motions, indicated by negative correlation centers, are primarily located in the northeastern coast of the AS and a larger area covering the southeastern AS, South India and the southern BoB (Figure 13e). In June, strong ascending motion is mainly visible over the entire Gangetic Plain along the Himalayan foothills and a weak descending motion to its northeast over the northern Indus Plain and adjacent west slopes of the TP (Figure 13f).

When comparing the 500-hPa vertical velocity correlations maps (Figures 13e and 13f) to the precipitation ones (Figures 7a–7d), one can see that the excessive rainfall centers almost overlapped to the above-mentioned ascending motion centers both in May and June. But compared the velocity correlation maps (Figures 13e and 13f) to those of air temperature (Figures 13c and 13d), the anomalous ascending motion centers are partially overlapped with the warming regions. It can also be seen that the ascending motion in the northeastern coast of AS (Figure 13e) intrudes into the warming region (Figure 13c) from southwest to the lower Indus Plain and the Thar Desert regions in May while the ascending motion in the upper Gangetic Plain overlapped with the southern part of the air warming area. The aerosol accumulations on the northeastern AS coast in May (Figure 5g) and North India Himalayan foothills in June (Figure 5h) have an in-phase trend with the aerosol loading over the AS, and climatologically the dust-forced radiative heating plays a significant warm effect in above anomalous warming regions (Wang et al., 2020; Xu et al., 2018; Yuan et al., 2019). This evidence suggests that, besides the regional impact from the diabetic heating in the southern part and weak descending motion in the northern part, the heating involves the rising-motion-induced semi-direct effect of the absorbing aerosols proposed by Lau and Kim (2006). Lau et al. (2006) is also one of the important contributors to the air temperature warming at 500 hPa. The processes that impact the above air temperature anomalies will be further discussed in the following sections.

It is also notable that the anomalous ascending motion associated with the AS increased aerosol loading in South India-southern BoB (Figure 13e) in May is generally opposite to those for the aerosol loading over the BoB (Figure 9e), and in June ascending motion is observed both in India and the northern SCS (Figure 13f). These exhibit a distinct circulation pattern that differs from the case for an increased aerosol loading over the BoB in which a significantly zonal overturning of Walker Circulation is dominant. In contrast to that, ascending motion is observed both in India and the northern SCS.

Figure 14 displays the correlations between the SST and AVHRR AOT or Terra AOD indices over the AS, respectively. The SST correlation patterns during 1983–2020 are different from that during 2000–2020 for the

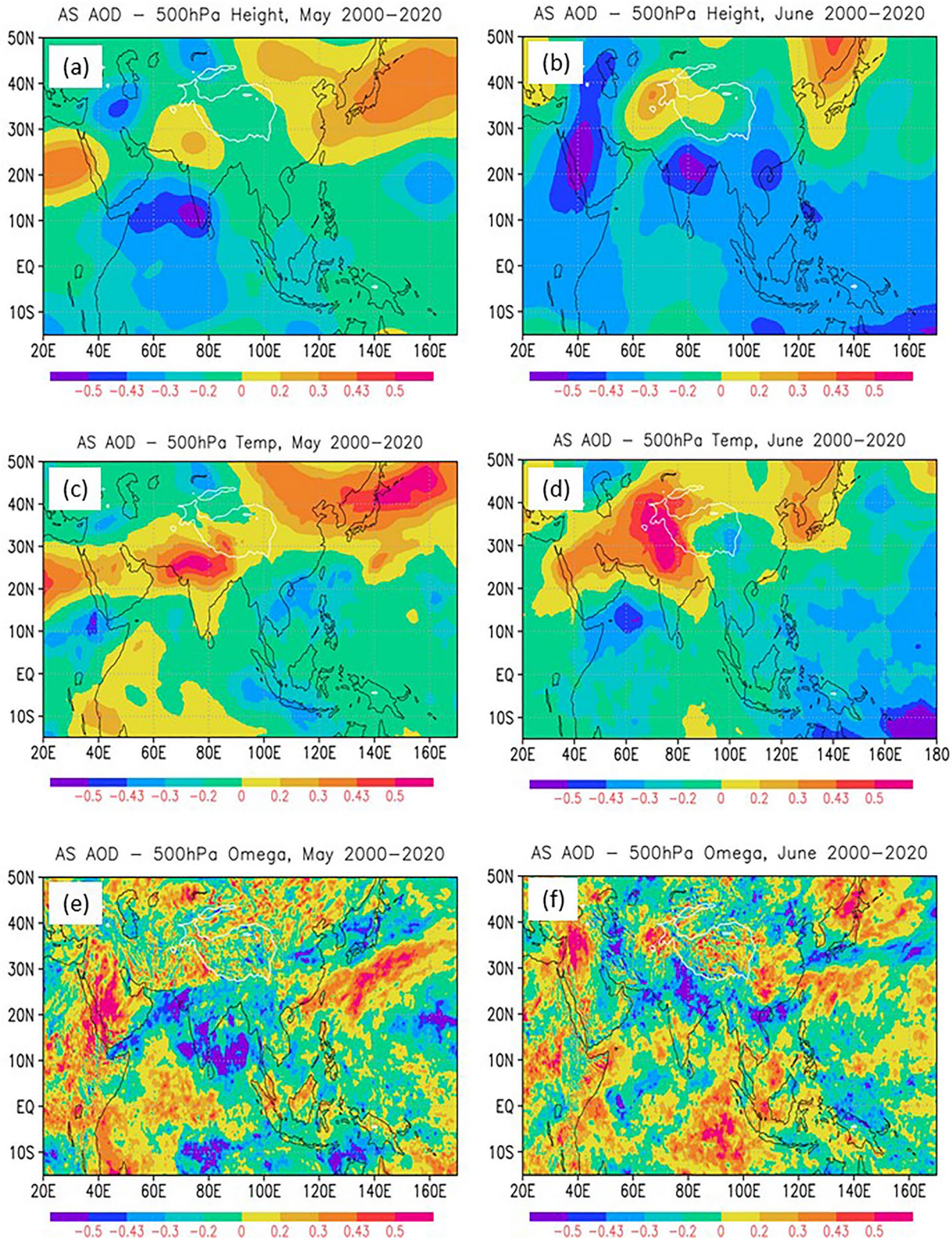

Figure 13. Same as Figure 9, but for the correlations of 500-hPa height, air temperature, and vertical velocity with respect to the Terra aerosol optical depth (AOD) over the Arabian Sea. White contour denotes the 3,000-m elevation of the Tibetan Plateau.

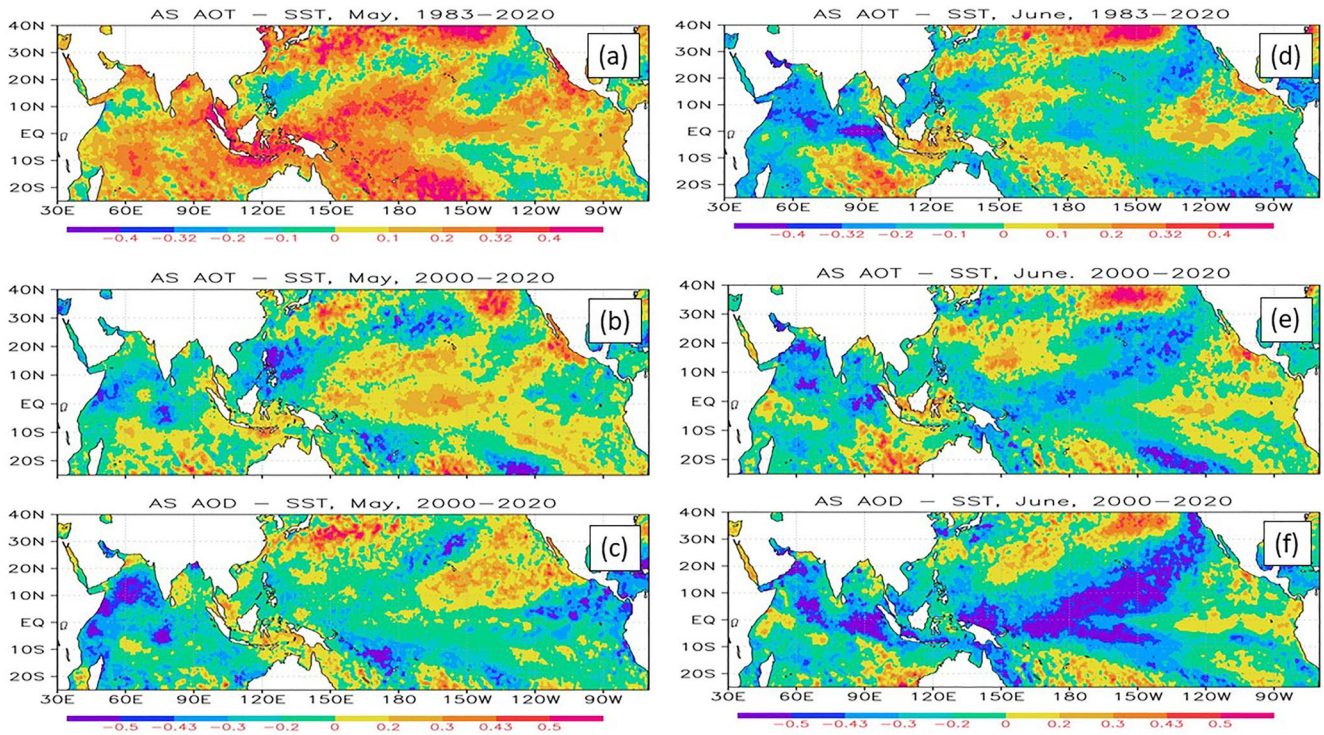

Figure 14. Same as Figure 10, but with respect to the aerosol indices over the Arabian Sea.

AVHRR AOT data in May. The former presents broad warm SSTA in the eastern Indian Ocean, the western Pacific Ocean, and the eastern Pacific Ocean (Figure 14a), while the latter only displays warm SSTA in the eastern Pacific Ocean (Figure 14b). During 2000–2020, both AVHRR AOT and Terra AOD indices exhibit a negative correlation of SST in the central-western Indian Ocean while minimum centers are located in the central Indian Ocean and the southern AS (Figures 14b and 14c). In Figures 14c and 14a significant SST cooling in the offshore coast of East Africa and the southern AS is concurrent with an enhancement of cross-equatorial flow in the region (Figure 12a) and significantly increased aerosol loading in the region (Figures 5c and 5g). Moreover, a small-size SST cooling is also observed in the central-equatorial Indian Ocean and accompanied by intensified westerly winds (Figure 12a). Therefore, an intensification of the upwelling might be attributed to the sea surface cooling, along with an in-phase of aerosol dimming effect, especially over the offshore coast of East Africa and the southern AS. During 1983–2020, the above correlation of AOT and surface wind disappeared which may partially explain why the relationship between SST and aerosol over the AS and southern India only exists during 2000–2020.

In June, significantly negative correlations between SST and aerosol are visible in the eastern and western equatorial Indian Ocean, respectively (Figures 14d–14f). The negative correlations are also visible in the northern AS whereas the signals for the AVHRR AOT during 1983–2020 are weaker. Compared to the 850-hPa wind anomalies shown in Figures 11c and 12b, the SST cooling centers in the Indian Ocean are concurrent with the strengthening of the prevailing winds. Significantly negative correlations between SST and Terra AOD index are also observed in the western equatorial Pacific Ocean and extend northeastward reaching the coast of North America at around 40°N. While a similar pattern is also observed between SST and AVHRR AOT, the signals are relatively weaker. It is also notable that the broadly distributed cold SSTA in the equatorial Indian-western Pacific Oceans between 5°S and 10°N latitude in Figure 14f is coincident with the occurrence of heavy loading of aerosol in these regions in Figure 5d. This suggests possible contribution of the aerosol dimming effect due to an increased aerosol loading to the cooling of the SST.

6.2. Physical Processes Underlying the Aerosol-Monsoon Interactions in the AS and Their Relationship to Indian Monsoon Rainfall Anomalies

Based on the above discussions, we can conclude that the dominant low-level convergence associated with the 850-hPa anomalous cyclonic circulation in the northern Arabian Sea exerts a direct effect upon the trapping of aerosol in the Arabian Sea. This feature is readily observed both in May (Figure 12a) and June (Figure 12b), whereas there is a slight north-south shift of location between those 2 months. At 200 hPa, the concurrence of the divergence associated with the anomalous anticyclonic circulation (Figures 12c and 12d) centered in the south of the Iran-Afghanistan-Pakistan regions strengthens the low-level convergence and middle-level ascending motion (Figures 13b and 13d), while the anomalous anticyclonic circulation center is located both along 65°E and at 30°N in May and 35°N in June. Coherently, the 850-hPa cyclonic cells in May and June, though with a shift in the location, bring in the aerosol emitted from the different regions in May and June, respectively. The former is primarily transported from the neighboring coastal regions of northwest India, the Arabian Peninsula, as well as East Africa where a strengthened cross-equatorial flow occurs in Somalia, the latter is mainly transported from the Arabian Peninsula.

The strong local air-sea interactions are also documented as being related to an increased aerosol loading over the AS. The local enhanced prevailing westerly or southwesterly winds not only lead to a cold SSTA in the region but also provide more aerosol emissions by producing more marine aerosols such as sea salt and sulfates. Moreover, the cold SSTA close to the coast of the eastern African and southern AS in May and in the equatorial Indian-West Pacific Ocean between 5°S and 10°N latitude in June are concurrent with heavy loading of aerosol in these regions, which implies that the dimming effect due to increased aerosol has also contributed to the cooling of the ocean surface. This leads to an increase in the meridional air temperature gradient between south Asia and the tropical Indian Ocean, which intensifies the low-level monsoonal southerly or southwesterly winds flowing into the Indian subcontinent.

In May for an increased aerosol loading over the AS, the development of the cyclonic circulation zone is visibly elongated from the northeastern AS to the southwest BoB and is accompanied by the anomalous low-level cross-equatorial southwesterly winds off the coast of East Africa and reversed flows at 200 hPa, as well as a lower pressure zone at 500 hPa. As a result, excessive monsoon rainfall is found along the southeastern AS-South Indian regions (Figure 7c).

In June, the anomalous southwesterly winds pass the Arabian Peninsula and meet the cross-equatorial flow between 60°E and 75°E in southeastern AS and extend to the Gangetic Plain (Figure 12b). Partially due to the topographic forcing of the Himalayas Mountain, the direction of winds changes from southwesterly to southeasterly along the Himalayan Foothills, which contributes to the development of a northwest-southeast-tilted trough and triggers strong ascending motion along the Himalayan Foothills (Figure 13f). In the upper level, intensified anomalous southward flow occurs over the region of 75°E–95°E and 25°N–45°N, which is associated with the anomalous anticyclonic cell in the southeastern Central Asia and a cyclonic one centered in the eastern TP. This upper-level southward flow changes from northerly to northeasterly in the northern BoB and easterly in the northwestern India, stimulating strong divergence. The combination of the low-level convergence and upper-level divergence, as well as topographic effects, brings about an enhanced arising motion (Figure 13f) that benefits an excessive monsoon rainfall in North India along the Himalayan Foothills (Figures 7b and 7d).

It is very interesting to note that an anomalous aerosol loading over the AS is in-phase with the aerosol change in the NIHF observed by Aqua land AOD data (Figure 5h), and the circulation and rainfall revealed in June resemble what has been documented by Lau and Kim (2006) and Lau et al. (2006, 2008). In their study, the upward motion in the southern slope of TP is proposed to be associated with the semi-direct aerosol effect of the absorbing aerosols originating from the elevated air pollution of India and dust from the nearby deserts, thereby inducing a large-scale upper-level heating anomaly over the TP in the early summer, and thus, reinforcing the meridional temperature gradient and intensifying the monsoon over India in June. Additionally, Gautam et al. (2009) consistently reported widespread warming over the Himalayan-Gangetic region and consequent strengthening of the land-sea thermal gradient. Comparing the distribution of the correlation maps between the aerosol over the AS and 500 hPa air temperature (Figure 13d) and vertical velocity (Figure 13f), one can see that the northwestern part of the air warming center (Figure 13d) coincides with a descending motion but its southeast part concurs with an ascending motion (Figure 13f). This implies that, in spite of being part of the large-scale remote teleconnection component that will be further discussed later, the anonymous warm air temperature over the NIHF is likely triggered by the combination of regional effects of descending flow in the northern part and elevated heat pump in the southern part of the warming region.

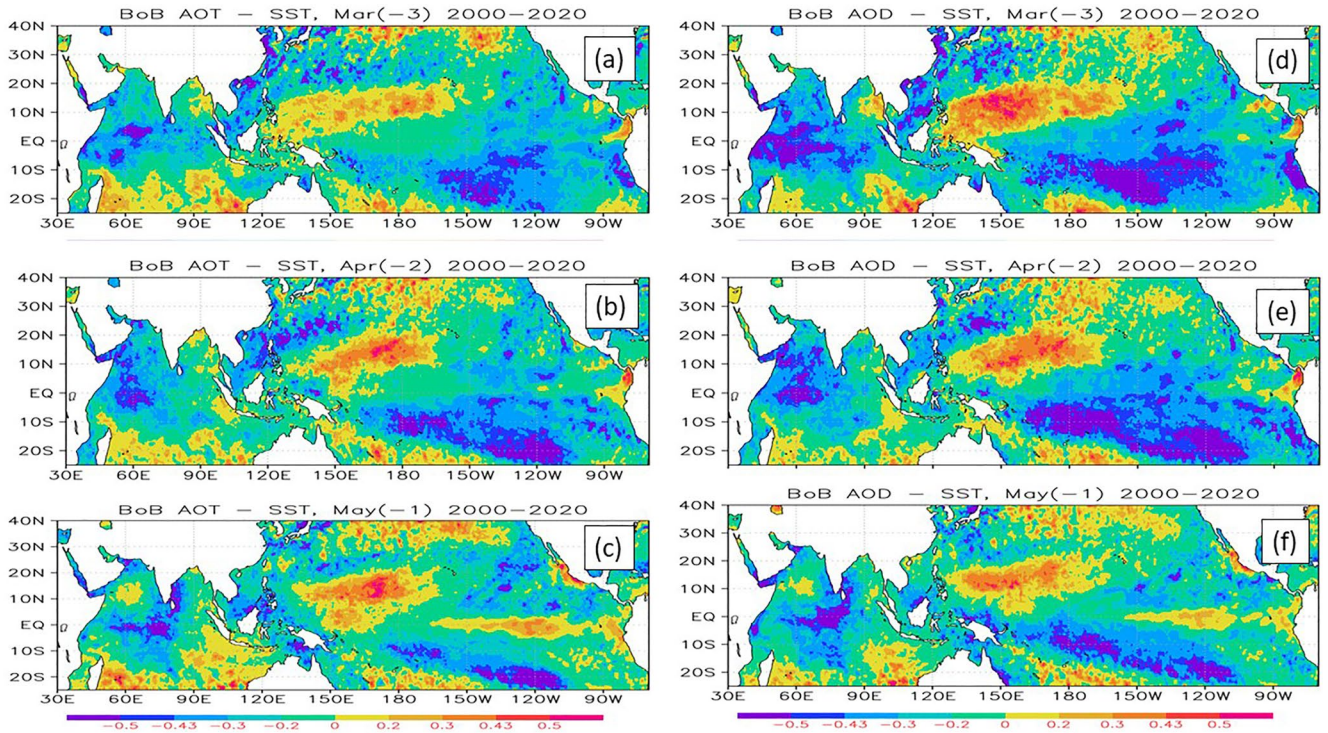

Figure 15. Left: Lagged Correlations between the Advanced Very High-Resolution Radiometer Bay of Bengal aerosol optical thickness (AVHRR BoB AOT) index in June and the sea surface temperature (SST) in the prior months from March to May. Right: Same as right, but with respect to the Terra BoB aerosol optical depth (AOD) index. March (−3), April (−2), and May (−1) denote the prior months and numbers refer to the reference month (June). The shading areas with values larger than 0.43 or smaller than −0.43 are exceeding 95% significance.

7. Precursory Signals of SST Anomaly in the Indian Ocean and Its Role in the Aerosol-Monsoon Interactions

In the previous sections, we indicate that the environmental atmospheric circulation for increased aerosol loadings over the BoB and AS in May and June are associated with a strengthening of aerosol transport from their upstream land regions and a favorable location lower-level trapping convergence that likely cool the ocean surface by the aerosol dimming effect. They are also concurrent with strong local air-sea interaction between the enhanced surface wind and underlying SST in which a strong upwelling cools the SST. These variations in atmospheric circulation and SST may exert an impact on the monsoon rainfall anomalies in India as well as Southeast and East Asia through a combination of remote forcing and the local effect. However, these analyses have not yielded a complete explanation of how the environmental atmospheric circulation for an increased or decreased aerosol loading over the BoB and the AS is induced and sustained, and especially what role the SSTA play in the modulation of the changes in monsoon circulation and anomalous aerosol accumulation.

Figure 15 displays the lagged correlations of aerosol indices over the BoB in June to the SST in the prior months from March to May. It is shown that the anomalous aerosol loading over the BoB in June is negatively correlated to the SST in the tropic western and central Indian Ocean with a slight eastward migration from the coast of East Africa to 80°E from March to May, and they can be observed in both AVHRR (Figures 15a–15c) and Terra data (Figure 15c, d, f). This negative relationship passes the 95% significance test whereas the signals observed from Terra AOD are slightly stronger. In the northwestern Pacific Ocean, a northeast-southwest-oriented positive correlation center is found extending from the southern Philippines Sea to the dateline and south of 20°N, and to its northern and southern sides, accompanied by two negative zones in the SCS-northeastern Philippine Sea extending to the western subtropical Pacific Ocean and the southern Pacific Ocean, respectively. The latter consists of a northwest-southeast-oriented band located between the equator to 20°S and 170°W to 100°W. Compared to those in the Indian Ocean, signals of the cold SST in the northwestern Pacific Ocean are relatively weaker.

Figure 16 presents the lagged correlation between the Terra AOD index over the AS in June and SST from prior months. We also calculated the correlation of SST to the AVHRR AOT index, but without showing the results here as they are similar to each other. A basin-wide SST cooling is observed in most of the Indian Ocean in the preceding March (Figure 16a) and in the central Indian Ocean between 55°E and 70°E in April (Figure 16b), while its shape changes to a zonal belt in the central and eastern equatorial Indian Ocean in May (Figure 16c). In the meantime, a warm SSTA has been observed in the northwestern Pacific Ocean centered around 155°E and 15°N and the strength of signal reduces gradually from March to May (Figure 16), fading away in June (Figure 14f). The cold SSTA is also visible in the equatorial eastern Pacific Ocean extending from the dateline to 120°W and between 10°S and 15°N.

The above results clearly demonstrate that an increased aerosol loading over the BoB and AS in June is preceded by a strong cold SST anomaly in the Indian Ocean. For further analysis, Figure 17 displays the lagged correlations between the aerosol indices in June and SST in the tropic western Indian Ocean covering 55°E–80°E and 5°S–5°N starting from October of the preceding year to September of the current year. The cold SSTA signals for an increased aerosol loading over the BoB in June from AVHRR AOT (blue solid line) and Terra AOD (blue dashed line), can be traced back to December in the preceding year, and readily persists to May whereas a weakening occurs in February. The results for AVHRR and Terra are quite similar to each other. Figure S6 in Supporting Information S1 shows that a negative correlation between aerosol over the BoB in May and SST in the equatorial western Indian Ocean can also be seen clearly in the preceding March and April. For an increased aerosol loading over the AS in June, the correlations are presented by red lines, and a notable cold SST anomaly is seen starting from March to May for both the Terra AOD (red dashed line) and AVHRR AOT (red solid line). However, only the correlations to the Terra AOD data have passed the 95% significance test.

Figure 18 presents lagged correlation between the Terra AOD index over the BoB in June and the 500-hPa air temperature (left panels) and height (right panels) in the preceding months from March to May, as well as June. It is shown that, as a correspondence to the cold SSTA, an increased aerosol loading over the BoB in June is preceded by a strong middle-level air cooling zone in the southeastern AS, the southern BoB, and North SCS in the preceding March (Figure 18a), which also presents as part of the northwest-southeast-tilted teleconnection pattern crossing the coast of northern AS to Central Asia. In April, the anomalous cold air temperature sustains and extends northward reaching the coast of North AS (Figure 18b), and persisting until May (Figure 18c). In June, two separate cool centers are visible in the central AS, and the coastal Northwest BoB, respectively.

As we have described in the previous sections, during the transitional season of the ASM, its timing in the northern Indian Ocean and South Asia is characterized by the establishment of summer tropical prevailing atmospheric circulation and tropical convection. It primarily includes northward retreatment of the subtropical westerlies which are replaced by northward tropical southwesterly winds over Indian land, the establishment of the cross-equatorial southwesterly winds offshore the coast of East Africa, as well as northward migration of the rainfall belt primarily situated in the BoB, India, and the Arabian Sea. While the interhemispheric thermal contrast resulting from differential solar radiation is the primary mechanism that drives large-scale seasonal changes in circulation and rainfall, the spatial distribution of thermal condition and thermal contrast between the ocean and continent is also crucial in the determination of the regionality of the timing of the ASM. Figures 18a–18d show that for an increased aerosol loading over the BoB in June how the middle-level cold atmosphere, which is also a reflection of the later retreat of the winter monsoon, is maintained in the northwestern Indian Ocean from early spring to the early summer in response to the cold SSTA in the Indian Ocean (Figure 15). This is also accompanied coherently by the humidity (Figures 9c and 9d) and wind fields (Figure 8), in which a dry atmosphere is favorable for more aerosol emission and stronger low-level subtropical westerly winds intensify the aerosol transport to the downstream BoB regions. On the other hand, the strong up-welling associated with the enhanced subtropical westerly winds and the aerosol dimming effect (due to increased aerosol loading) tends to cause a cold SST in the northern Indian Ocean, which not only suppresses the generation of onset vortex but also in turn reinforces the reduction of the meridional temperature gradient between the subtropical region and the equatorial Indian Ocean. The latter benefits the delayed development of the cross-equatorial southwesterly winds offshore the coast of eastern Africa. These factors favor a delayed arrival of the Asian summer monsoon in South Asia.

In 500-hP height fields, Figure 18e exhibits a teleconnection pattern similar to that of the air temperature (Figure 18a) as the high (low) pressure center corresponds to the warm (cold) centers and vice versa. Then, anomalous low-pressure centers are visible along the coast of North AS from April to May (Figures 18f and 18g).

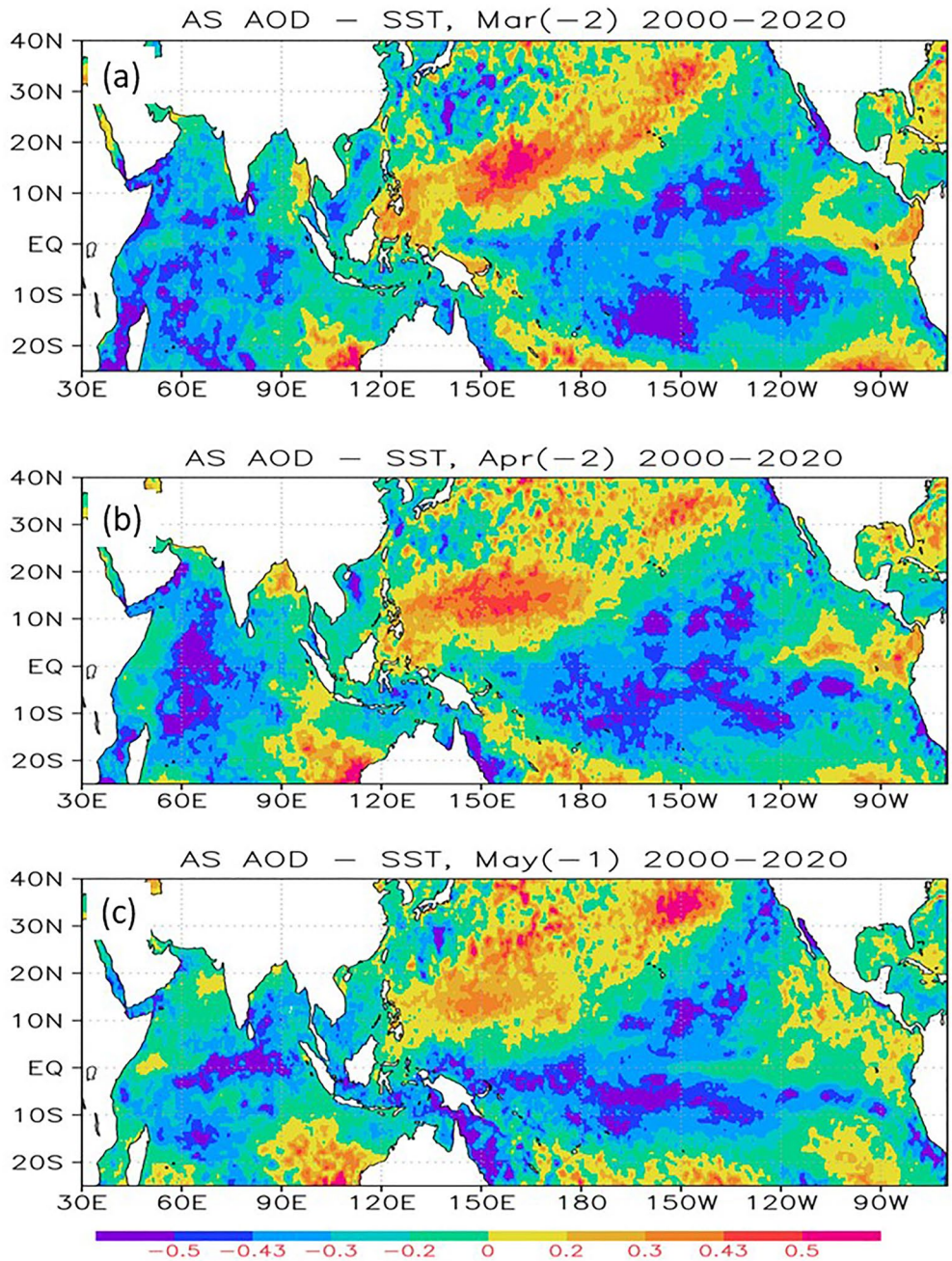

Figure 16. Same as Figure 15, but with respect to the Terra aerosol optical depth (AOD) index over the Arabian Sea.

In May, a wide significantly anomalous low-pressure zone is found in the tropical Indian and Pacific Oceans (Figure 18g), and consistently reflects a weaker and eastward retreat of the western North Pacific subtropical high which is closely related to the tropical convective activity situated in the SCS (Chang et al., 2000a, 2000b; Wang et al., 2001). In June, an anomalous low-pressure zone appears extending from the northeastern BoB-Southern slope of TP to North SCS between 15°N and 30°N latitude (Figure 18h) and are overlapped with a weak-warm center (Figure 18d). Conversely, a pattern of high-pressure center versus cold center is observed in June over the northern AS, which is different from the configuration of low-pressure center versus cold center for the dry winter monsoon condition in March. Dynamically, this anomalous low pressure over southern TP helps the development of low-level subtropical northwesterly winds in the Indian peninsula for a strengthened aerosol transport and deepening of the BBT which favors a trapping of the aerosol over the BoB. As we have discussed previously,

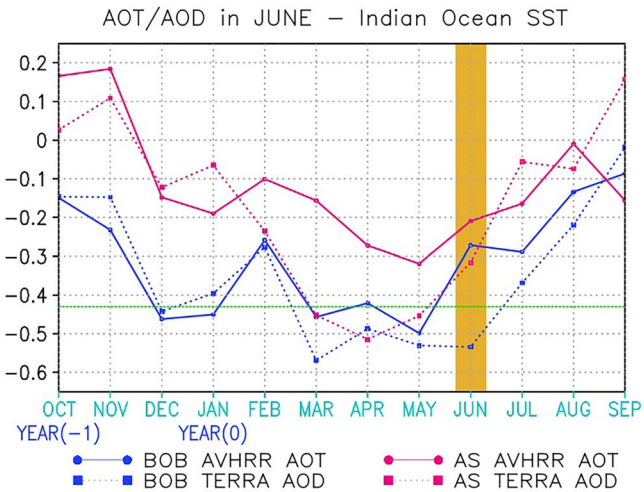

Figure 17. Lagged correlations between the aerosol anomaly in Bay of Bengal (BoB) (blue lines) and Arabian Sea (AS) (red lines) in June observed from Advanced Very High-Resolution Radiometer (AVHRR) (solid lines) and Terra (dashed lines) and the sea surface temperature (SST) anomaly in the western Indian Ocean (55°E–80°E, 5°S–5°N), YEAR (−1) and YEAR (0) refer to the year before and the reference year, respectively. The dashed horizontal green lines indicate a correlation of 95% confidence level. The yellow vertical bar marks the reference month.

referring to the detailed analysis by Chang et al. (2000a, 2000b) for a similar pattern but forced primarily by the ENSO, a low-pressure zone in the northern SCS implies an interannual eastward retreat of the western North Pacific subtropical high which is modulated by the diabetic heating of the convection and is favorable for the development of 850-hPa anomalous cyclone off the coast of the southeastern China. The latter, along with the cold SSTA in the SCS and BoB, and a southward invasion of the vortex from the higher latitude due to the weakening of the western North Pacific subtropical high, exerts an important impact on the drought over the regions extending from southwestern China to the Huaihe River Basin, and vice versa.

Similar to Figure 18, Figure 19 presents the lagged correlation between the Terra AOD index over the AS in June and the 500-hPa air temperature and height in the prior months. Compared to what has been involved in the aerosol loading over the BoB, the relationship between the aerosol loading over the AS and SST changes in the Indian Ocean and the associated monsoon rainfall anomaly is more complicated and subtler. While noticeable cold air temperature anomalies at 500 hPa, reflected by the highly negative correlations, are visible from preceding March to May in the western Indian Ocean (Figures 19a–19c) and the southern AS in June (Figure 19d), those over South Asian land exhibit completely different features since the preceding May. From preceding March to April, air temperature anomalies in the northwestern Indian Ocean are likely part of seesaw variations between the subtropical Indian-west Pacific Ocean and middle-latitude regions in the Northern Hemisphere. Two cold centers in the northern Indian Ocean and the northwestern Pacific Ocean are observed and concurrent with two weak warm ones to their north in Central Asia and Northeast Siberia, respectively. However, in the preceding May significant warm temperature anomalies start to occur in South Asia as part of a teleconnection pattern which is characterized by a northeast-southwest-oriented wave train spanning the southern India-western Indian Ocean, the northwestern TP, the northeastern Asia and the northeastern Siberia (Figure 19c). In June, the warm temperature anomalies move southwestward from the northwestern TP to North Indus Plain-Gangetic Plain along the Himalayan foothills while the cold temperature anomalies only confine to the southern AS (Figure 19d). Corresponding to an increased meridional temperature gradient between South Asia and the northern Indian Ocean owed to dominant warming in the northern Indus Plain-Gangetic Plain and the SST cooling in the western Indian Ocean, strong cross-equatorial southerly winds are stimulated in the northern Indian Ocean in the longitude domain from 65°E to 75°E (Figures 11d and 12b), providing sufficient water vapor supply favoring excessive monsoon rainfall in North India along the Himalayan Foothills.

The correlation maps between 500-hPa height fields and the AS aerosol index (Figures 19f–19h) are consistent with the evolution of the air temperature anomalies from spring to early summer (Figures 19b–19d). Furthermore, low-pressure anomalies that benefit the development of the monsoon trough in the region are readily visible along the NIHF in both May and June. Therefore, as a direct impact factor, the evolution of the 500-hPa anomalous air temperature and height field suggests that a remote teleconnection pattern associated with the SST changes in the Indian Ocean plays an important role in the development of the excessive monsoon rainfall in northern India in June.

It is notable in this study that while a remote teleconnection of large-scale circulation driven primarily by the Indian Ocean SST anomalies remarkably stimulates the favorable background, the regional three-dimensional circulation, and India monsoon rainfall distributions associated with the aerosol-monsoon interactions over the AS exhibit some similar features which have been documented by Lau and Kim (2006) and Lau et al. (2006, 2008). Using the Atmospheric Radiative Transfer model and 10-year Cloud-Aerosol Lidar and Infrared Pathfinder Satellite Observation (CALIPSO), Wang et al. (2020) pointed out that the Indus Plain and Gangetic Plain are among those where the climatic average of the dust-forced radiative heating (DRH) at the near-surface is 3–3.6 times warmer than the column-average from spring to summer. In these regions, the aerosol-induced elevated heat pump proposed by Lau and Kim (2006) and Lau et al. (2006, 2008) may work as a regional effect to reinforce the air temperature. This conclusion is also supported by recent studies (e.g., Xu et al., 2018; Yuan et al., 2019) that

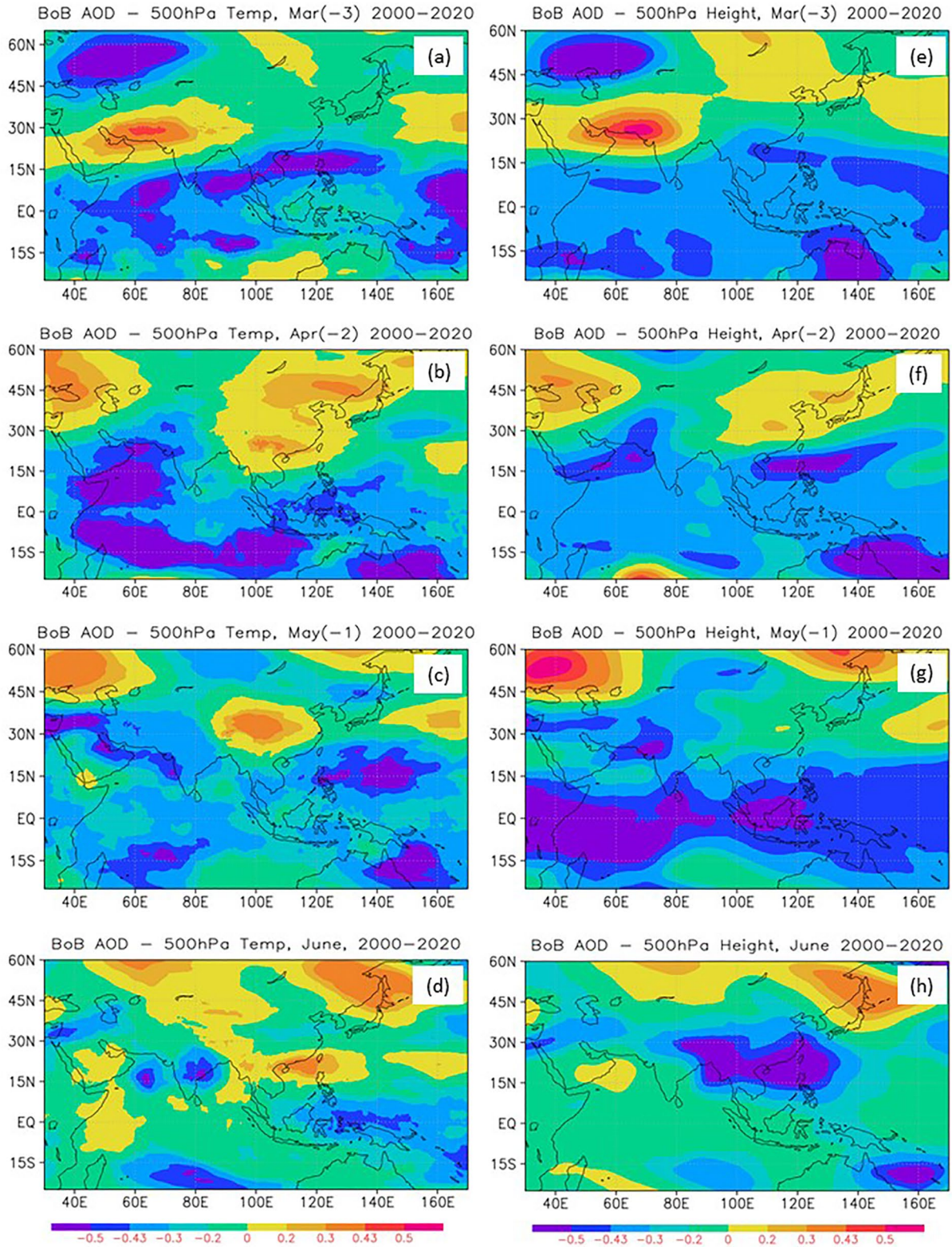

Figure 18. Left: Lagged correlations between the Terra aerosol optical depth (AOD) over the Bay of Bengal (BoB) in June and the 500-hPa air temperature in the prior months from March to May. Right: Same as right, but with respect to the 500-hPa geopotential height. March (−3), April (−2), and May (−1) denote the prior months and numbers refer to the reference month (June). The shading areas with values larger than 0.43 or smaller than −0.43 are exceeding 95% significance.

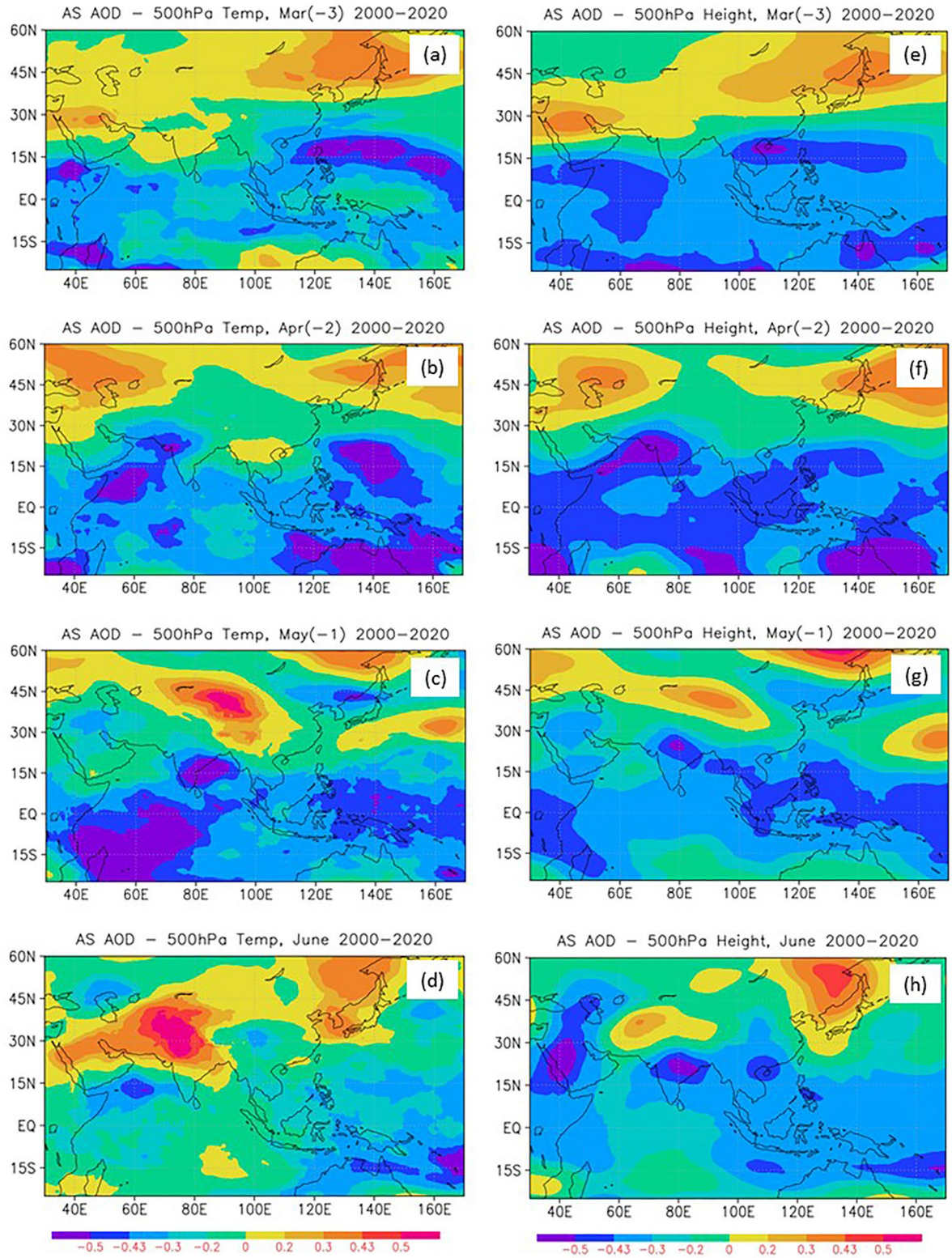

Figure 19. Same as Fig. 18, but with respect to the Terra aerosol optical depth (AOD) over the Arabian Sea.

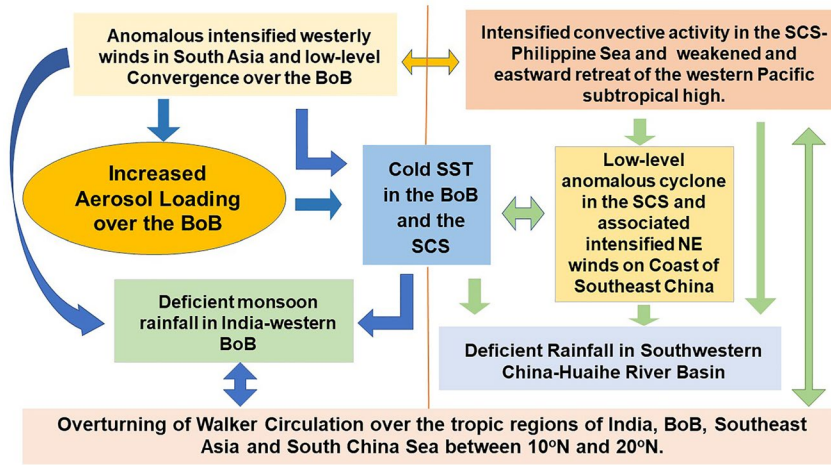

Figure 20. Schematic diagram showing the primary physical processes that are associated the interactions between the increased aerosol loading over the Bay of Bengal (BoB) and South Asian monsoon (left part with blue arrows) and East and East Asian monsoon (right part with green arrows) in June.

investigated the dynamic and thermal impact of TP on the dust aerosols transport over the regions adjacent to the northwest TP, and indicated that dry convection prevailing over the western TP could uplift the dust aerosols to the upper troposphere during the spring and early summer.

8. Summary and Discussions

Based on the satellite-observed aerosol from the NOAA AVHRR instrument from 1983 and MODIS Terra products from 2000 to the present, we explore the interannual relationship between the anomalous aerosol loadings over the BoB and the AS and Asian monsoon rainfall anomalies in the boreal early summer and their association with the SST anomalies in the Indian Ocean. In the first part of this study, our comparison analyses present the consistency of the annual and interannual variability of the aerosol products between AVHRR AOT and Terra AOD products over the BoB and the AS in May and June. We also confirm that the two data sets describe similar temporal-spatial features in the relationship between the anomalous aerosol loadings over the BoB and the AS and monsoon circulation variations during 2000–2020.

Our study identifies that the strong low-level aerosol transport through southerly or southwesterly winds primarily from the Indian subcontinent, the local trapping effect associated with the development of BBT, and the low-level meridional convergence along the northwestern coast of the BoB are responsible for an increased aerosol loading over the BoB in May, and vice versa. In June strong low-level aerosol transport by intensified westerly winds from the northern Arabian Sea to the Indian subcontinent becomes dominant. Furthermore, the intensified surface-prevailing westerly winds in the BoB also lead to further production of local marine aerosol by increasing the sea salt flux from the ocean to the atmosphere both in May and June. A dry atmospheric background in northwestern India benefits increased emissions of aerosol in the Indian land and Arabian Peninsula. The above features are schematically presented in Figure 20, which exhibits the primary physical processes involving the interactions between the increased aerosol loading over the BoB and Asian monsoon in June. These processes also exist in May whereas their locations are generally situated southward in contrast to those in June, as a reflection of the northward migration of the South Asian monsoon from the BoB to North India, as well as the East Asian monsoon from the SCS to North China.

It is shown that when an increased (decreased) aerosol loading is observed over the BoB, a deficient (excessive) rainfall is primarily observed in the regions extending from the northeastern India, Bangladesh to the northern Myanmar in May, and in the central and the southern Indian subcontinent in June, implying a dry (wet) or delayed (earlier) arrival of Indian monsoon rainfall in these regions. Moreover, these monsoon rainfall anomalies concur with suppressed (intensified) convections in the southeastern BoB and the central-eastern tropic Indian Ocean and intensified (suppressed) ones in the SCS-Philippine Sea. The associated changes of horizontal wind fields at 850 and 200 hPa, and 500-hPa vertical velocity and height suggest an overturning of the east-west Walker

Circulation between the southwestern BoB and the SCS-Philippine Sea along the tropical region between 10°N and 20°N latitude. In Southeast and East Asia, the intensified (suppressed) convections in the SCS-Philippine Sea display also as part of the north-south-oriented large-scale anomalous rainfall teleconnection pattern which propagates northward with alternating signs from the equator to the middle latitude. Among these dry or wet centers, a distinct dry (wet) monsoon rainfall appears extending from southwestern China to the Huaihe River Basin in June. The existence of an anomalous cyclone (anticyclone) cell on the coast of Southeast China plays an important role in the determination of the monsoon rainfall anomalies in East Asia. A noticeable associated reduction (enhancement) of the prevailing southwesterly winds occurs in South and Southwestern China and leads to a lower (higher) moisture supply from the BoB and the SCS to the land. Therefore, deficient (excessive) summer monsoon rainfall appears in the southwestern China and Huaihe River Basin.

The above driving physical processes contain the most important circulation systems which modulate the changes of the East Asian summer monsoon rainfall associated to the occurrence of the ENSO (Chang et al., 2000a, 2000b; Wang et al., 2000) whereas the ENSO signals of the SSTA in the tropical central-eastern Pacific Ocean are very weak in our study. However, the impacted geographic domain stretches southwest-northeastward from Southwest China and eastern North China covering the Huaihe River Basin, rather than a straight north-south displacement between the Southeast Coast and the low Yangtze River Valley. Our study, presents that, while the ENSO signal is very weak (Figure 10), such anomalous cyclonic or anticyclonic circulation can still be triggered by the combination of intense convective activity in SCS to its south, an eastward retreat of the western North Pacific subtropical ridge as well as a strong cold (warm) SSTA in the SCS.

Similar to previous but using different satellite aerosol data sets during a longer time period, this study also reveals that an increased aerosol loading over the Arabian Sea is primarily due to the dust transport from the Arabian Peninsula and neighboring land by anomalous westerly or southwesterly winds, a trapping effect by the low-level anomalous cyclonic circulation over the AS, as well as more local marine aerosols emissions by enhanced local prevailing winds associated with the Somali Jet. This study implies that, while the role of enhanced prevailing winds could not be ignored, the aerosol dimming effect due to increased aerosol also contributes to the cooling of the SST close to the coast of the eastern African and southern AS in May and in the equatorial Indian-West Pacific Ocean between 5°S and 10°N latitude in June.

An increased aerosol loading over the AS is highly correlated to enhanced monsoon rainfall in South India in May and North India along the Himalayan foothills in June, and vice versa. For an increased aerosol loading over the AS, anomalous cyclonic circulation at 200 hPa is dominant in the northeastern India along 65°E with a north-south shift from 30°N in May to 35°N in June at 200 hPa, accompanied by 500-hPa air warming in the southern Indus Plain-Thar Desert which is partially intensified by the semi-direct aerosol effect of the absorbing aerosols in June (Lau & Kim, 2006; Lau et al., 2006). The latter reinforces the meridional temperature gradient between the land and the equatorial Indian Ocean, thereby inducing anomalous strong low-level cross-equatorial southwesterly winds off the coast of East Africa. Along with reversed flows at 200 hPa, excessive monsoon rainfall occurs over the eastern AS-South Indian regions and vice versa. In June, the anomalous southwesterly winds prevail in the Arabian Peninsula and meet the cross-equatorial flow between 60°E and 75°E in southeastern AS and extend to the Gangetic Plain. A northwest-southeast-tilted trough then forms and triggers strong ascending motion along the Himalayan Foothills by topographic forcing which induces air temperature warming combined with the semi-direct aerosol effect of the absorbing aerosols. These factors tend to contribute to excessive monsoon rainfall in North India.

This study also finds that the increased (decreased) aerosol loading over the BoB and the AS in June is preceded by the cold (warm) SSTA in the equatorial western Indian Ocean from the preceding winter to early summer of the current year. But the evolution of simulated atmospheric circulation changes and monsoon-aerosol interactions over these two regions differ distinctly, and result in different summer monsoon rainfall anomalies. For an increased aerosol loading over the BoB, the cold air temperature at 500 hPa driven by the cold SST is maintained in the western Indian Ocean and the coast of northern AS in the early spring. It moves to the Indian subcontinent in June and tends to either sustain a dry winter Asian monsoon or delay the arrival of the wet summer monsoon, which contributes greater aerosol emission and transport through enhanced subtropical westerly winds. The SST cooling due to the enhanced westerly winds which intensify ocean upwellings and aerosol dimming effect in the BoB and the SCS in turn benefits a weaker ASM in India in June. For an increased aerosol loading over the AS, while the cold air temperature at 500 hPa driven by the cold SST is maintained in the western Indian

Ocean and the coast of northern AS in the early spring, warm air temperature anomalies occur as a component of the stimulated teleconnection pattern and aerosol absorb heating in the NIHF. This reinforces the meridional temperature gradient between the land and ocean in the northern Indian Ocean, and thereby, strengthens the low-level cross-equatorial southwesterly winds flowing into the Indian Peninsula, driving a strong summer monsoon there.

It is notable that the above interannual relationship between aerosol loadings over the BoB and the Arabian Sea and Asian monsoon rainfall anomalies in early summer and the role of SST anomalies in the Indian Ocean are dominant primarily during the time period of 2000–2020, where they are observed significantly both by AVHRR and MODIS Terra products. The change in the long-term background of the atmospheric circulation might be one of the key factors causing the weakening of the aerosol-monsoon relationship for the whole time period of 1983–2020. In East Asia, compared to those during 2000–2020 for an increased loading of aerosol over the BoB, the strength of the anomalous westerly winds in the tropic northeastern Indian Ocean, the SCS, and west Phillippe Sea and anomalous cyclonic circulation along the coast of Southeast China are much weaker during 1983–2020 (Figure 8d and Figure S4b in Supporting Information S1), therefore the impacted area is smaller and mainly located in the southwestern North China. Similarly, the anomalous westerly or northwesterly winds are relatively weaker in North India and the western BoB as is the cold SSTA over the BoB (Figure 10d). These may partially account for a weaker monsoon rainfall anomaly along the coast of eastern India (Figure 7f and Figure S4b in Supporting Information S1).

For an increased loading of the aerosol over the AS in June, the BBT is stronger and located far northward on the coast of northern BoB during 2000–2020 (Figures 11c and 12b) compared to this during 1983–2020 which is primarily observed on the coast of the southwestern BoB (Figure 11d). Associatively, stronger anomalous southwesterly winds are observed in the NIHF during 2000–2020 while only westerly winds prevail mainly to south India south of 20°N altitude during 1983–2020 (Figure 11d). Therefore, more northward transport with increased loading of aerosol, along with stronger moisture supply to its south, ensures the occurrence of the "elevated heat pump (EHP)" which is associated with the semi-direct aerosol effect of the absorbing aerosols proposed by Lau and Kim (2006) and Lau et al. (2006). Some clues in recent studies indicate that monsoon rainfall has increased in India since early 2000 (Jin & Wang, 2017; Sanap & Pandithurai, 2014), and that a summertime dust amplification has been occurring over the Arabian Peninsula for about the past two decades (Ravi Kumar et al., 2019). Therefore, an in-depth investigation of aerosol interdecadal variation over the AS and BoB, along with more complex methods in a broader geographic domain is needed and is going to be pursued in separate studies.

Data Availability Statement

The AVHRR AOT CDR is downloaded at NCEI via Zhao and NOAA CDR Program (2017). The MODIS monthly global products contain the data from the Terra and the Aqua and are downloaded from the NASA GIOVANNI website via Platnick et al. (2015). The SeaWiFS deep blue Level 3 monthly product is also downloaded from the NASA GIOVANNI website via Hsu et al. (2013). ERA5 data are downloaded through the Climate Data Store of Copernicus Climate Change Service via Hersbach et al. (2019). The GPCC monthly precipitation is downloaded from the NOAA Physical Sciences Laboratory (PSL) via Schamm et al. (2014). The GPCP monthly precipitation is downloaded from NOAA PSL via Adler et al. (2016). The monthly OISST V2.1 data is downloaded from NCEI via Huang et al. (2020).

Acknowledgments
This study was supported by the NOAA Grant NA19NES4320002 (Cooperative Institute for Satellite Earth System Studies-CISESS) at the University of Maryland/ESSIC. Drs. Zhao and Zhang are supported by NCEI base fund. Three anonymous reviewers' comments and suggestions are constructive for the improvement of the paper. NCEI internal review provided by Drs. Boyin Huang and Saha Korak and proofreading of the paper by English editor Laura Ohlmann and Lukas Noguchi of NCEI are greatly appreciated. GPCP and GPCC monthly precipitation data are provided by the NOAA/OAR/ESRL PSL, Boulder, Colorado, USA, from their website at https://psl.noaa.gov.

References

Adler, R., Wang, J.-J., Sapiano, M., Huffman, G., Chiu, L., Xie, P. P., et al. (2016). Global Precipitation Climatology Project (GPCP) Climate Data Record (CDR), version 2.3 (monthly). *National Centers for Environmental Information*. [Dataset]. https://doi.org/10.7289/V56971M6

Albrecht, B. A. (1989). Aerosols, cloud microphysics, and fractional cloudiness. *Science*, *245*(4923), 1227–1230. https://doi.org/10.1126/science.245.4923.1227

Ashok, K., Guan, Z., & Yamagata, T. (2001). Impact of the Indian Ocean dipole on the relationship between the Indian monsoon rainfall and ENSO. *Geophysical Research Letters*, *28*(23), 4499–4502. https://doi.org/10.1029/2001GL013294

Bamzai, A. S., & Shukla, J. (1999). Relation between Eurasian snow cover, snow depth, and the Indian summer monsoon: An observational study. *Journal of Climate*, *12*(10), 3117–3132. https://doi.org/10.1175/1520-0442(1999)012<3117:RBESCS>2.0.CO;2

Bollasina, M., Ming, Y., & Ramaswamy, V. (2011). Anthropogenic aerosols and the weakening of the South Asian summer monsoon. *Science*, *334*(6055), 502–505. https://doi.org/10.1126/science.1204994

Breon, F. M., Tanre, D., & Generoso, S. (2002). Aerosol effect on cloud droplet size monitored from satellite. *Science*, *295*(5556), 834–838. https://doi.org/10.1126/science.1066434

Cao, C., Xiong, X., Wu, A., & Wu, X. (2008). Assessing the consistency of AVHRR and MODIS L1B reflectance for generating fundamental climate data records. *Journal of Geophysical Research*, *113*(D9), D09114. https://doi.org/10.1029/2007JD009363

Chang, C. P., Zhang, Y., & Li, T. (2000a). Interannual and interdecadal variations of the East Asian summer monsoon and tropical Pacific SSTs: Part I: Role of subtropical ridges. *Journal of Climate*, *13*(24), 4310–4325. https://doi.org/10.1175/1520-0442(2000)013<4310:IAIVOT>2.0.CO;2

Chang, C. P., Zhang, Y., & Li, T. (2000b). Interannual and interdecadal variations of the East Asian summer monsoon and tropical Pacific SSTs: Part II: Meridional structure of the monsoon. *Journal of Climate*, *13*(24), 4326–4340. https://doi.org/10.1175/1520-0442(2000)013<4326:IAIVOT>2.0.CO;2.,

Chen, G. T., & Chang, C.-P. (1980). Structure and vorticity budget of early summer monsoon trough (Mei-Yu) over southeastern China and Japan. *Monthly Weather Review*, *108*(7), 942–953. https://doi.org/10.1175/1520-0493(1980)108<0942:TSAVBO>2.0.CO;2

Chen, L., & Wu, R. (2000). Interannual and decadal variations of snow cover over Qinghai-Xizang Plateau and their relationships to summer monsoon rainfall in China. *Advances in Atmospheric Sciences*, *17*(1), 18–30. https://doi.org/10.1007/s00376-000-0040-7

Coakley, J. A., Bernstein, R. R., & Durkee, P. A. (1987). Effect of ship-stack effluents on cloud reflectivity. *Science*, *237*(4818), 1020–1022. https://doi.org/10.1126/science.237.4818.1020

Ding, Y. H. (1992). Summer monsoon rainfalls in China. *Journal of the Meteorological Society of Japan*, *70*(1B), 373–396. https://doi.org/10.2151/jmsj1965.70.1b_373

Gandham, H., Dasari, H. P., Ashok, K., Ravuri, P. M. K., & Hoteit, I. (2022). Three-dimensional structure and transport pathways of dust aerosols over West Asia. *npj Climate and Atmospheric Science*, *5*(1), 45. https://doi.org/10.1038/s41612-022-00266-2

Gandham, H., Dasari, H. P., Langodan, S., Karumuri, R. K., & Hoteit, I. (2020). Major changes in extreme dust events dynamics over the Arabian Peninsula during 2003–2017 driven by atmospheric conditions. *Journal of Geophysical Research: Atmospheres*, *125*(24), e2020JD032931. https://doi.org/10.1029/2020JD032931

Ganguly, D., Rasch, P. J., Wang, H., & Yoon, J.-H. (2012). Climate response of the South Asian monsoon system to anthropogenic aerosols. *Journal of Geophysical Research*, *117*(D13), D13209. https://doi.org/10.1029/2012JD017508.,

Gautam, R., Hsu, N. C., Lau, K. M., Tsay, S. C., & Kafatos, M. (2009). Enhanced pre-monsoon warming over the Himalayan-Gangetic region from 1979 to 2007. *Geophysical Research Letters*, *36*(7), L07704. https://doi.org/10.1029/2009GL037641

Gordon, H. R., & Wang, M. (1994). Retrieval of water-leaving radiance and aerosol optical thickness over the oceans with Sea-WiFS: A preliminary algorithm. *Applied Optics*, *33*(3), 443–452. https://doi.org/10.1364/AO.33.000443

Hahn, D. G., & Shukla, J. (1976). Apparent relationship between Eurasian snow cover and Indian monsoon rainfall. *Journal of the Atmospheric Sciences*, *33*(12), 2461–2462. https://doi.org/10.1175/1520-0469(1976)033<2461:AARBES>2.0.CO;2

Heidinger, A. K., Cao, C., & Sullivan, J. T. (2002). Using Moderate Resolution Imaging Spectrometer (MODIS) to calibrate advanced very high resolution radiometer reflectance channels. *Journal of Geophysical Research*, *107*(D23). https://doi.org/10.1029/2001JD002035

Heidinger, A. K., Foster, M. J., Walther, A., Zhao, X.-P., & NOAA CDR Program. (2014). *NOAA Climate Data Record (CDR) of Cloud Properties from AVHRR Pathfinder Atmospheres - Extended (PATMOS-x), Version 5.3*. NOAA National Centers for Environmental Information. https://doi.org/10.7289/V5348HCK

Heidinger, A. K., Straka, W. C., III, Molling, C. C., Sullivan, J. T., & Wu, X. (2010). Deriving an inter-sensor consistent calibration for the AVHRR solar reflectance data record. *International Journal of Remote Sensing*, *31*(24), 6493–6517. https://doi.org/10.1080/01431161.2010.496472

Hersbach, H., Bell, B., Berrisford, P., Biavati, G., Horányi, A., Muñoz Sabater, J., et al. (2019). ERA5 monthly averaged data on pressure levels from 1959 to present. [Dataset]. Copernicus Climate Change Service (C3S) Climate Data Store (CDS). https://doi.org/10.24381/cds.6860a573

Hersbach, H., Bell, B., Berrisford, P., Hirahara, S., Horanyi, A., Munoz-Sabater, J., et al. (2020). The ERA5 global reanalysis. *Quarterly Journal of the Royal Meteorological Society*, *146*(730), 1–51. https://doi.org/10.1002/qj.3803

Hsu, N. C., Sayer, A. M., Jeong, M.-J., & Bettenhausen, C. (2013). SeaWiFS Deep Blue Aerosol Optical Depth and Angstrom Exponent Monthly Level 3 Data Gridded at 1.0 Degrees V004 [Dataset]. *Goddard Earth Sciences Data and Information Services Center (GES DISC)*. https://doi.org/10.5067/MEASURES/SWDB/DATA304

Hsu, N. C., Tsay, S.-C., King, M. D., & Herman, J. R. (2006). Deep blue retrievals of Asian aerosol properties during ACE-Asia. *IEEE Transactions on Geoscience and Remote Sensing*, *44*(11), 3180–3195. https://doi.org/10.1109/TGRS.2006.879540

Huang, B., Liu, C., Banzon, V., Freeman, E., Graham, G., Hankins, B., et al. (2020). NOAA 0.25-degree Daily Optimum Interpolation Sea Surface Temperature (OISST), version 2.1. [Dataset]. *NOAA National Centers for Environmental Information*. https://doi.org/10.25921/RE9P-PT57

Huang, B., Liu, C., Banzon, V., Freeman, E., Graham, G., Hankins, B., et al. (2021). Improvements of the Daily Optimum Interpolation Sea Surface Temperature (DOISST) version 2.1. *Journal of Climate*, *34*(8), 2923–2939. https://doi.org/10.1175/JCLI-D-20-0166.1

IPCC. (2021). In V., Masson-Delmotte, P., Zhai, V. A., Pirani, S. L., Connors, C., Péan, et al. (Eds.), *Climate change 2021: The physical science basis. Contribution of working group I to the sixth assessment report of the intergovernmental panel on climate change*. Cambridge University Press. in press. https://doi.org/10.1017/9781009157896

Jeong, M. J., & Li, Z. Q. (2005). Quality, compatibility, and synergy analyses of global aerosol products derived from the advanced very high resolution radiometer and Total Ozone Mapping Spectrometer. *Journal of Geophysical Research*, *110*(D10), D10S08. https://doi.org/10.1029/2004JD004647

Jin, Q., & Wang, C. A. (2017). Revival of Indian summer monsoon rainfall since 2002. *Nature Climate Change*, *7*(8), 587–594. https://doi.org/10.1038/nclimate3348

Jin, Q., Wei, J., Lau, W. K. M., Pu, B., & Wang, C. (2021). Interactions of Asian mineral dust with Indian summer monsoon: Recent advances and challenges. *Earth-Science Reviews*, *215*, 103562. https://doi.org/10.1016/j.earscirev.2021.103562

Jin, Q., Wei, J., & Yang, & Z.-L. (2014). Positive response of Indian summer rainfall to Middle East dust. *Geophysical Research Letters*, *41*(11), 4068–4074. https://doi.org/10.1002/2014GL059980

Jin, Q., Wei, J., Yang, Z.-L., Pu, B., & Huang, J. (2015). Consistent response of Indian summer monsoon to Middle East dust in observations and simulations. *Atmospheric Chemistry and Physics*, *15*(17), 9897–9915. https://doi.org/10.5194/acp-15-9897-2015

Johnson, R. H., Wang, Z., & Bresch, J. F. (1993). Heat and moisture budgets over China during the early summer monsoon. *Journal of the Meteorological Society of Japan Ser. II.*, *71*(1), 137–152. https://doi.org/10.2151/jmsj1965.71.1_137

Kaskaoutis, D. G., Houssos, E. E., Solmon, F., Legrand, M., Rashki, A., Dumka, U., et al. (2018). Impact of atmospheric circulation types on southwest Asian dust and Indian summer monsoon rainfall. *Atmospheric Research*, *201*, 189–205. https://doi.org/10.1016/j.atmosres.2017.11.002

Kaufman, Y. J., Tanré, D., Remer, L. A., Vermote, E. F., Chu, A., & Holben, B. N. (1997). Operational remote sensing of tropospheric aerosol over land from EOS moderate resolution imaging spectroradiometer. *Journal of Geophysical Research*, *102*(D14), 17051–17067. https://doi.org/10.1029/96JD03988

Krishnamurti, T. N., Jha, B., Prospero, J., Jayaraman, A., & Ramanathan, V. (1998). Aerosol and pollutant transport and their impact on radiative forcing over the tropical Indian Ocean during the January–February 1996 pre-INDOEX cruise. *Tellus Series B*, *50*(5), 521–542. https://doi.org/10.3402/tellusb.v50i5.16235

Kumar, K., Rajagopalan, K. B., & Cane, M. A. (1999). On the weakening relationship between the Indian monsoon and ENSO. *Science*, *284*(5423), 2156–2159. https://doi.org/10.1126/science.284.5423.2156

Lau, K. M., & Kim, K. M. (2006). Observational relationships between aerosol and Asian monsoon rainfall, and circulation. *Geophysical Research Letters*, *33*(21), L21810. https://doi.org/10.1029/2006GL027546

Lau, K. M., Kim, M.-K., & Kim, K. M. (2006). Asian summer monsoon anomalies induced by aerosol direct forcing: The role of the Tibetan Plateau. *Climate Dynamics*, *26*(7–8), 855–864. https://doi.org/10.1007/s00382-006-0114-z

Lau, K. M., Ramanathan, V., Wu, G. X., Li, Z., Tsay, S. C., Hsu, C., et al. (2008). The joint aerosol–monsoon experiment: A new challenge for monsoon climate research. *Bulletin of the American Meteorological Society*, *89*(3), 369–384. https://doi.org/10.1175/BAMS-89-3-369

Lau, K.-M., & Yang, S. (1997). Climatology and interannual variability of the Southeast Asian summer monsoon. *Advances in Atmospheric Sciences*, *14*(2), 141–162. https://doi.org/10.1007/s00376-997-0016-y

Levy, R. C., Remer, L. A., & Dubovik, O. (2007a). Global aerosol optical properties and application to Moderate Resolution Imaging Spectroradiometer aerosol retrieval over land. *Journal of Geophysical Research*, *112*(D13), D13210. https://doi.org/10.1029/2006JD007815

Levy, R. C., Remer, L. A., & Dubovik, O. (2007b). Second-generation algorithm for retrieving aerosol properties over land from MODIS spectral reflectance. *Journal of Geophysical Research*, *112*, D13211. https://doi.org/10.1029/2006JD007811.,

Li, T., Wang, B., Chang, C. P., & Zhang, Y. (2003). A theory for the Indian Ocean dipole–zonal mode. *Journal of the Atmospheric Sciences*, *60*(17), 2119–2135. https://doi.org/10.1175/1520-0469(2003)060<2119:ATFTIO>2.0.CO;2

Li, Z., Lau, W. K., Ramanathan, V., Wu, G., Ding, Y., Manoj, M. G., et al. (2016). Aerosol and monsoon climate interactions over Asia. *Review of Geophysics*, *54*(4), 866–929. https://doi.org/10.1002/2015RG000500

Li, Z., Zhao, X., Kahn, R., Mishchenko, M., Remer, L., Lee, K.-H., et al. (2009). Uncertainties in satellite remote sensing of aerosols and impact on monitoring its long-term trend: A review and perspective. *Annales Geophysicae*, *27*(7), 2755–2770. https://doi.org/10.5194/angeo-27-2755-2009

Lohmann, U., & Feichter, J. (2005). Global indirect aerosol effects: A review. *Atmospheric Chemistry and Physics*, *5*(3), 715–737. https://doi.org/10.5194/acp-5-715-2005

Madhavan, B. L., Niranjan, K., Sreekanth, V., Sarin, M. M., & Sudheer, A. K. (2008). Aerosol characterization during the summer monsoon period over a tropical coastal Indian station, Visakhapatnam. *Journal of Geophysical Research*, *113*(D21), D21208. https://doi.org/10.1029/2008JD010272

Massie, T. S., Torres, O., & Smith, S. J. (2004). Total ozone mapping spectrometer (TOMS) observations of increases in Asian aerosol in winter from 1979 to 2000. *Journal of Geophysical Research*, *109*(D18), D18211. https://doi.org/10.1029/2004JD004620

Meehl, G. A., Arblaster, J., & Collins, W. (2008). Effects of black carbon aerosols on the Indian monsoon. *Journal of Climate*, *21*(12), 2869–2882. https://doi.org/10.1175/2007JCLI1777.1

Menon, S., Hansen, J., Nazarenko, L., & Luo, Y. (2002). Climate effects of black carbon aerosols in China and India. *Science*, *297*(5590), 2250–2253. https://doi.org/10.1126/science.1075159

Mishchenko, M., & Geogdzhayev, I. V. (2007). Satellite remote sensing reveals regional tropospheric aerosol trends. *Optics Express*, *15*(12), 7423–7438. https://doi.org/10.1364/oe.15.007423

Moorthy, K. K., & Satheesh, S. K. (2000). Characteristics of aerosols over a remote island, Minicoy in the Arabian Sea: Optical properties and retrieved size characteristics. *Quarterly Journal of the Royal Meteorological Society*, *126*(562), 81–109. https://doi.org/10.1002/qj.49712656205

Ohmura, A. (2009). Observed decadal variations in surface solar radiation and their causes. *Journal of Geophysical Research*, *114*, D00D05. https://doi.org/10.1029/2008JD011290

Platnick, S., et al. (2015). MODIS Atmosphere L3 Monthly Product [Dataset]. *NASA MODIS Adaptive Processing System, Goddard Space Flight Center*. https://doi.org/10.5067/MODIS/MOD08_M3.006

Ramanathan, V., Chung, C., Kim, D., Bettge, T., Buja, L., Kiehl, J. T., et al. (2005). Atmospheric brown clouds: Impacts on South Asian climate and hydrological cycle. In *Proceedings of the National Academy of Sciences* (Vol. 102, pp. 5326–5333). https://doi.org/10.1073/pnas.0500656102

Ramanathan, V., Crutzen, P. J., Kiehl, J. T., & Rosenfeld, D. (2001). Aerosols, climate, and the hydrological cycle. *Science*, *294*(5549), 2119–2124. https://doi.org/10.1126/science.1064034.,

Ramanathan, V., Crutzen, P. J., Lelieveld, J., Mitra, A. P., Althausen, D., Anderson, J., et al. (2001). Indian Ocean Experiment: An integrated analysis of the climate forcing and effects of the great Indo-Asian haze. *Journal of Geophysical Research*, *106*(D22), 28371–28398. https://doi.org/10.1029/2001JD900133

Ravi Kumar, K., Attada, R., Dasari, H. P., Vellore, R. K., Abualnaja, Y. O., Ashok, K., & Hoteit, I. (2019). On the recent amplification of dust over the Arabian Peninsula during 2002–2012. *Journal of Geophysical Research: Atmospheres*, *124*(23), 13220–13229. https://doi.org/10.1029/2019JD030695

Remer, L. A., Kaufman, Y. J., Tanré, D., Mattoo, S., Chu, D. A., Martins, J. V., et al. (2005). The MODIS aerosol algorithm, products, and validation. *Journal of the Atmospheric Sciences*, *62*(4), 947–973. https://doi.org/10.1175/JAS3385.1

Remer, L. A., Kleidman, R. G., Levy, R. C., Kaufman, Y. J., Tanré, D., Mattoo, S., et al. (2008). Global aerosol climatology from the MODIS satellite sensors. *Journal of Geophysical Research*, *113*(D14), D14S07. https://doi.org/10.1029/2007JD009661

Reynolds, R. W., Rayner, N. A., Smith, T. M., Stokes, D. C., & Wang, W. (2002). An improved in situ and satellite SST analysis for climate. *Journal of Climate*, *15*(13), 1609–1625. https://doi.org/10.1175/1520-0442(2002)015<1609:AIISAS>2.0.CO;2

Rosenfeld, D., Lohmann, U., Raga, G. B., O'Dowd, C. D., Kulmala, M., Fuzzi, S., et al. (2008). Flood or drought: How do aerosols affect precipitation? *Science*, *321*(5894), 1309–1313. https://doi.org/10.1126/science.1160606

Saji, N., Goswami, B., Vinayachandran, P., & Yamagata, T. (1999). A dipole mode in the tropical Indian Ocean. *Nature*, *401*(6751), 360–363. https://doi.org/10.1038/43854

Sanap, S. D., & Pandithurai, G. (2014). Inter-annual variability of aerosols and its relationship with regional climate over Indian subcontinent. *International Journal of Climatology*, *5*(6), 1041–1053. https://doi.org/10.1002/joc.4037

Schamm, K., Ziese, M., Becker, A., Finger, P., Meyer-Christoffer, A., Schneider, U., et al. (2014). Global gridded precipitation over land: A description of the new GPCC first guess daily product [Dataset]. *Earth System Science Data*, *6*(1), 49–60. https://doi.org/10.5194/essd-6-49-2014

Seinfeld, J. H., Bretherton, C., Carslaw, K. S., Coe, H., DeMott, P. J., Dunlea, E. J., et al. (2016). Improving our fundamental understanding of the role of aerosol-cloud interactions in the climate system. *Proceedings of the National Academy of Sciences, USA*, *1113*(21), 5781–5790. https://doi.org/10.1073/pnas.1514043113

Slingo, J. (1999). The Indian summer monsoon and its variability. In A. Navarra (Ed.), *Beyond El Nino: Decadal variability in the climate system* (pp. 103–118). Springer-Verlag.

Tanaka, M. (1992). Intraseasonal oscillation and the onset and retreat dates of the summer monsoon over the east, southeast, and western North Pacific region using GMS high cloud amount data. *Journal of the Meteorological Society of Japan, Ser. II*, *70*(1B), 613–629. https://doi.org/10.2151/jmsj1965.70.1B_613

Tanré, D., Kaufman, Y. J., Herman, M., & Mattoo, S. (1997). Remote sensing of aerosol properties over oceans using the MODIS/EOS spectral radiances. *Journal of Geophysical Research*, *102*(D14), 16971–16988. https://doi.org/10.1029/96JD03437

Tao, S., & Chen, L. (1987). A review of recent research on the East Asian summer monsoon in China. In C.-P. Chang, & T. N. Krishnamurti (Eds.), *Monsoon Meteorology* (pp. 60–92). Oxford University Press.

Tian, B., Waliser, D. E., Kahn, R. A., Li, Q., Yung, Y. L., Tyranowski, T., et al. (2008). Does the Madden-Julian Oscillation influence aerosol variability? *Journal of Geophysical Research*, *113*(D12), D12215. https://doi.org/10.1029/2007JD009372.,

Twomey, S. (1974). Pollution and the planetary albedo. *Atmospheric Environment*, *8*(12), 1251–1256. https://doi.org/10.1016/0004-6981(74)90004-3

Vinoj, V., Rasch, P., Wang, H., Yoon, J. H., Ma, P. L., Landu, K., & Singh, B. (2014). Short-term modulation of Indian summer monsoon rainfall by West Asian dust. *Nature Geoscience*, *7*(4), 308–313. https://doi.org/10.1038/ngeo2107

Wang, B., & Lin, H. (2002). Rainy season of the Asian–Pacific summer monsoon. *Journal of Climate*, *15*(4), 386–398. https://doi.org/10.1175/1520-0442(2002)015<0386:RSOTAP>2.0.CO;2

Wang, B., Wu, R., & Fu, X. (2000). Pacific–East Asian teleconnection: How does ENSO affect East Asian climate? *Journal of Climate*, *13*(9), 1517–1536. https://doi.org/10.1175/1520-0442(2000)013<1517:PEATHD>2.0.CO;2

Wang, B., Wu, R., & Lau, K.-M. (2001). Interannual variability of the Asian summer monsoon: Contrasts between the Indian and the western North Pacific–East Asian monsoons. *Journal of Climate*, *14*(20), 4073–4090. https://doi.org/10.1175/1520-0442(2001)014<4073:IVOTAS>2.0.CO;2

Wang, C., Kim, D., Ekman, A. M. L., Barth, M. C., & Rasch, P. J. (2009). Impact of anthropogenic aerosols on Indian summer monsoon. *Geophysical Research Letters*, *36*(21), L21704. https://doi.org/10.1029/2009GL040114

Wang, T., Han, Y., Huang, J., Sun, M., Jian, B., Huang, Z., & Yan, H. (2020). Climatology of dust-forced radiative heating over the Tibetan Plateau and its surroundings. *Journal of Geophysical Research: Atmospheres*, *125*(17), e2020JD032942. https://doi.org/10.1029/2020JD032942

Webster, P. J., Magaña, V. O., Palmer, T. N., Shukla, J., Tomas, R. A., Yanai, M., & Yasunari, T. (1998). Monsoons: Processes, predictability, and the prospects for prediction. *Journal of Geophysical Research*, *103*(C7), 14451–14510. https://doi.org/10.1029/97JC02719

Wild, M., Trüssel, B., Ohmura, A., Long, C. N., König-Langlo, G., Dutton, E. G., & Tsvetkov, A. (2009). Global dimming and brightening: An update beyond 2000. *Journal of Geophysical Research*, *114*, D00D13. https://doi.org/10.1029/2008JD011382

Wu, G., Duan, A., Liu, Y., Mao, J., Ren, R., Bao, Q., et al. (2014). Tibetan plateau climate dynamics: Recent research progress and outlook. *National Science Review*, *2*(1), 100–116. https://doi.org/10.1093/nsr/nwu045

Wu, G., Guan, Y., Liu, Y., Yan, J., & Mao, J. (2012). Air–sea interaction and formation of the Asian summer monsoon onset vortex over the Bay of Bengal. *Climate Dynamics*, *38*(1), 261–279. https://doi.org/10.1007/s00382-010-0978-9

Wu, G., Ren, S., Xu, J., Wang, D., Bao, Q., Liu, B., et al. (2013). Impact of tropical cyclone development on the instability of South Asian High and the summer monsoon onset over Bay of Bengal. *Climate Dynamics*, *41*, 2603–2616. https://doi.org/10.1007/s00382-013-1766-0

Wu, G., & Zhang, Y. (1998). Tibetan Plateau forcing and the timing of the monsoon onset over South Asia and the South China Sea. *Monthly Weather Review*, *126*(4), 913–927. https://doi.org/10.1175/1520-0493(1998)126<0913:TPFATT>2.0.CO;2

Wu, T.-W., & Qian, Z.-A. (2003). The relation between the Tibetan winter snow and the Asian summer monsoon and rainfall: An observational investigation. *Journal of Climate*, *16*(12), 2038–2051. https://doi.org/10.1175/1520-0442(2003)016<2038:TRBTTW>2.0.CO;2

Xiao, Z., & Duan, A. (2016). Impacts of Tibetan plateau snow cover on the interannual variability of the East Asian summer monsoon. *Journal of Climate*, *29*(23), 8495–8514. https://doi.org/10.1175/JCLI-D-16-0029.1

Xu, C., Ma, Y., Yang, K., & You, C. (2018). Tibetan plateau impacts on global dust transport in the upper troposphere. *Journal of Climate*, *31*(12), 4745–4756. https://doi.org/10.1175/JCLI-D-17-0313.1

Xu, X., Guo, J., Koike, T., Liu, Y., Shi, X., Zhu, F., & Zhang, S. (2012). Downstream effect of winter snow cover over the eastern Tibetan Plateau on climate anomalies in East Asia. *Journal of the Meteorological Society of Japan, Ser. II*, *90C*(0), 113–130. https://doi.org/10.2151/jmsj.2012-C08

Yang, S., Lau, W. K. M., Ji, Z., Dong, W., & Yang, S. (2022). Impacts of radiative effect of pre-monsoon biomass burning aerosols on atmospheric circulation and rainfall over Southeast Asia and southern China. *Climate Dynamics*, *59*(1–2), 417–432. https://doi.org/10.1007/s00382-021-06135-7

Yasunari, T. (1990). Impact of Indian monsoon on the coupled atmosphere/ocean system in the tropical Pacific. *Meteorology and Atmospheric Physics*, *44*(1–4), 29–41. https://doi.org/10.1007/BF01026809

Yasunari, T., Kitoh, A., & Tokioka, T. (1991). Local and remote responses to excessive snow mass over Eurasia appearing in the northern spring and summer climate - A study with the MRI GCM. *Journal of the Meteorological Society of Japan. Ser. II*, *69*(4), 473–487. https://doi.org/10.2151/jmsj1965.69.4_473

Yuan, T., Chen, S., Huang, J., Wu, D., Lu, H., Zhang, G., et al. (2019). Influence of dynamic and thermal forcing on the meridional transport of Taklimakan desert dust in spring and summer. *Journal of Climate*, *32*(3), 749–767. https://doi.org/10.1175/JCLI-D-18-0361.1

Zhang, Y., Li, T., & Wang, B. (2004). Decadal change of the spring snow depth over the Tibetan plateau: The associated circulation and influence on the East Asian summer monsoon. *Journal of Climate*, *17*(14), 2780–2793. https://doi.org/10.1175/1520-0442(2004)017<2780:DCOTSS>2.0.CO;2

Zhao, P., Zhou, Z., & Liu, J. (2007). Variability of Tibetan spring snow and its associations with the hemispheric extratropical circulation and East Asian summer monsoon rainfall: An observational investigation. *Journal of Climate*, *20*(15), 3942–3955. https://doi.org/10.1175/JCLI4205.1.,

Zhao, T. X.-P., Dubovik, O., Smirnov, A., Holben, B. N., Sapper, J., Pietras, C., et al. (2004). Regional evaluation of an advanced very high-resolution radiometer (AVHRR) two-channel aerosol retrieval algorithm. *Journal of Geophysical Research*, *109*(D2), D02204. https://doi.org/10.1029/2003jd003817d

Zhao, T. X.-P., Laszlo, I., Guo, W., Heidinger, A., Cao, C., Jelenak, A., et al. (2008). Study of long-term trend in aerosol optical thickness observed from operational AVHRR satellite instrument. *Journal of Geophysical Research*, *113*(D7), D07201. https://doi.org/10.1029/2007JD009061

Zhao, T. X.-P., Laszlo, I., Holben, B. N., Pietras, C., & Voss, K. J. (2003). Validation of two-channel VIRS retrievals of aerosol optical thickness over the ocean and quantitative evaluation of the impact from potential subpixel cloud contamination and surface wind effect. *Journal of Geophysical Research*, *108*(D3). https://doi.org/10.1029/2002JD002346

Zhao, T. X.-P., Laszlo, I., Minnis, P., & Remer, L. (2005). Comparison and analysis of two aerosol retrievals over the ocean in the Terra/clouds and the Earth's radiant energy system - moderate resolution imaging spectroradiometer single scanner footprint data: 1. Global evaluation. *Journal of Geophysical Research*, *110*(D21), D21208. https://doi.org/10.1029/2005JD005851

Zhao, X.-P., & NOAA CDR Program. (2017). NOAA Climate Data Record (CDR) of AVHRR Daily and Monthly Aerosol Optical Thickness (AOT) over Global Oceans, Version 3.0 [Dataset]. *NOAA National Centers for Environmental Information*. https://doi.org/10.7289/V5BZ642P